Impact of seabed scour on the dynamics of bottom-founded offshore wind turbines with large diameter monopiles

Reeti Sarkar

Master Thesis Report
October 7, 2019
TU Delft

TUDelft

Impact of seabed scour on the dynamics of bottom-founded offshore wind turbines with large diameter monopiles

by

Reeti Sarkar

to obtain the degree of Master of Science
at the Delft University of Technology,
and Norway University of Technology and Sciences (NTNU)

Student number:	4344500	
Project duration:	September 15, 2018 - present	
Thesis committee:	Prof. Andrei Metrikine,	TU Delft, chair
	Dr. Federico Pisano,	TU Delft, supervisor
	Dr.Luke J. Prendegast,	supervisor (in absentia)
	Dr. Erin Bachynski,	NTNU, supervisor
	Evangelos Kemenzetzidis,	TU Delft, supervisor

TU Delft   EWEM   NTNU

Acknowledgments

This thesis has been a rather long journey, full of both frustrating moments and jubilant revelations. The compeltion of this journey however, would not be possible without the contributions of some very important people.

My supervisor Evangelos Kementzidis for his constant availability and interest: engaging with the most tedious computational queries and helping me burn through a lot of practical software matters in a very short time.

My supervisors Dr. Erin Bachynski, Dr. Federico Pisano, and Dr. LJ Prendergast, for supporting me each in their individual areas of expertise, and being available in any way possible: whether over video-conference or in person or over email.

My committee chair Prof. Andrei Metrikine, for his enthusiasm about the subject and providing introspective questions to help guide my thesis toward valuable conclusions.

All my friends for their moral support, and specifically my boyfriend for a lot of practical support as well, in the form of extra computational power and last minute LaTeXtutorials.

All the EWEM family and my own family, for allowing me to go through this very intense journey of over two years that culminates in this thesis.

<div align="right">

Reeti Sarkar
Delft, October 2019

</div>

Contents

List of Figures

List of Tables

1

Introduction

In recent years, the world has seen an increased drive towards renewable energy. In Europe in particular, the wind energy industry has seen rapid growth - and with the development of offshore wind turbines (OWTs), this growth has been accelerated even further.

1.1. Development of large OWTs

In going offshore, avenues have opened up for much larger turbines, as concerns over aesthetics and noise is greatly reduced. Additionally, the lower roughness of water as well as increased hub height of turbines ensures a much richer quality of wind resource offshore.
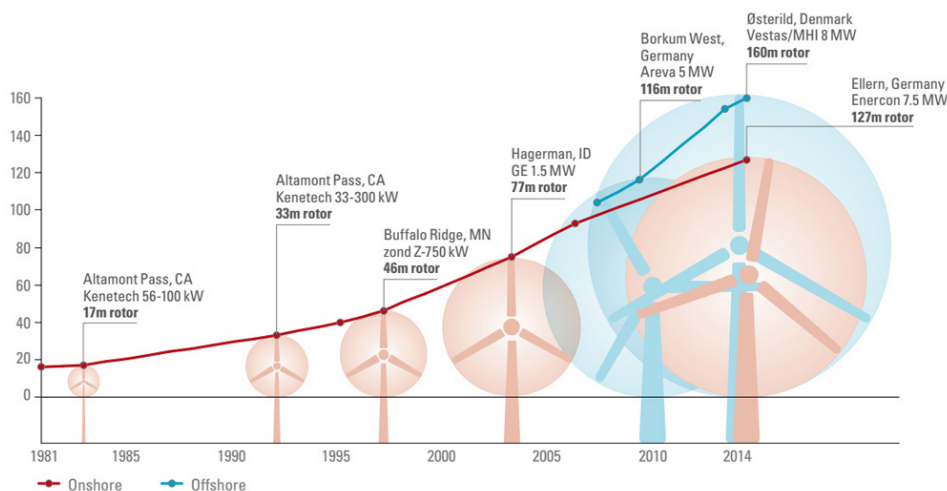
Figure 1.1: Trend for increase in rotor diameter. Source: [14]

The trend toward increase in rotor diameter has greatly accelerated in recent years. Figure 1.1 illustrates this trend; additionally, the Vestas 10 MW turbine and the GE Haliade-X have also been announced since the date of publication of this figure ([7], [6]).

It is expected that this trend will continue, as mega turbines of 15 or 20 MW capacity are developed [7]. However to support these turbines in the offshore conditions, a well developed foundation system is required. Unlike onshore conditions, design, fabrication and installation of offshore foundations is a much greater issue, especially due to cost and accessibility concerns. This will only increase with the trends of moving further offshore and into deeper waters, as illustrated by WindEurope ([37]) in figure 1.2. A large share of these turbines continue to be supported by monopile foundations.

1

1.2. Offshore foundations
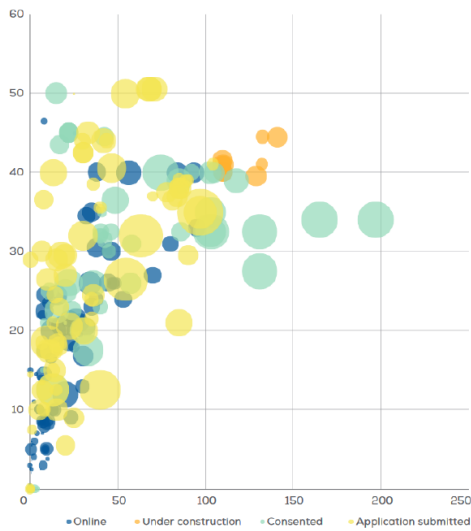
Figure 1.2: Trend of water depth and distance to shore in offshore wind farms. Source: WindEurope
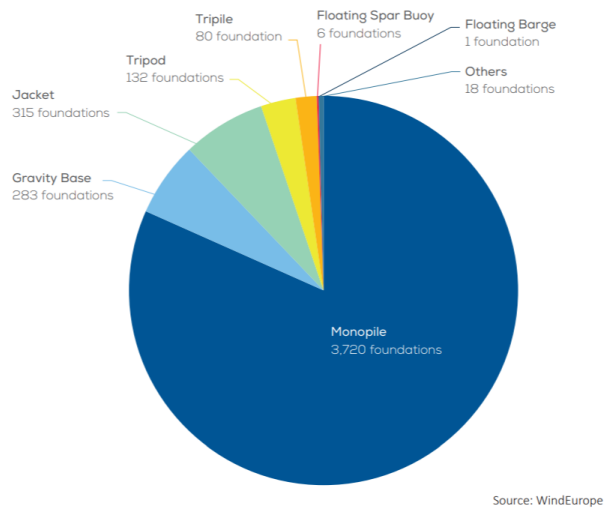
Figure 1.3: Share of substructures for grid-connected wind turbines. Source: [37]

Floating wind turbines are a good solution to combat the challenge of greater water depths. However it has not yet been deployed on a large scale commercial level. Therefore, bottom-fixed structures continue to dominate the current market. As the monopile is the most common bottom-fixed substructure, research into its design continues to be of great use.

In order to support the mega turbines however, mega monopiles of diameters in the range of 8-10 m are also being developed. However, this poses a problem in the design phase because a substantial portion of literature is based in studies of slender piles - which are no longer valid for piles of such large diameter. Thus, new studies are required to examine how these larger diameter monpiles are influenced by various environmental conditions, such as wave action, scour, etc. In the current project, it is intended to examine the influence of scour in particular, on such large diameter monopiles.

<div align="right">

2

</div>

Problem Analysis

The resonant frequency and lateral load capacity of an offshore wind turbine are vital aspects in its performance. The monopile faces largely lateral loading due to hydrodynamic forcing from waves, while there is large lateral aerodynamic force on the RNA and tower. Additionally, the resonance frequency of turbines with monopile foundations should generally be within the narrow soft-stiff range, which avoid both the 1P and 3P frequencies of the blades, as well as the wave period.

The stiffness of soil and embedded depth of the monopile have a substantial impact on these properties of the overall turbine. Both of these features are substantially impacted by the formation of scour.

2.1. Scour

Scour is the excavation and removal of sediment around a structure. It requires an imbalance in sediment transport [34]. In case of the ocean, scour occurs at the seabed and is influenced largely by tides and currents - and to a smaller extent, by wave action.

2.1.1. Mechanism of scour formation
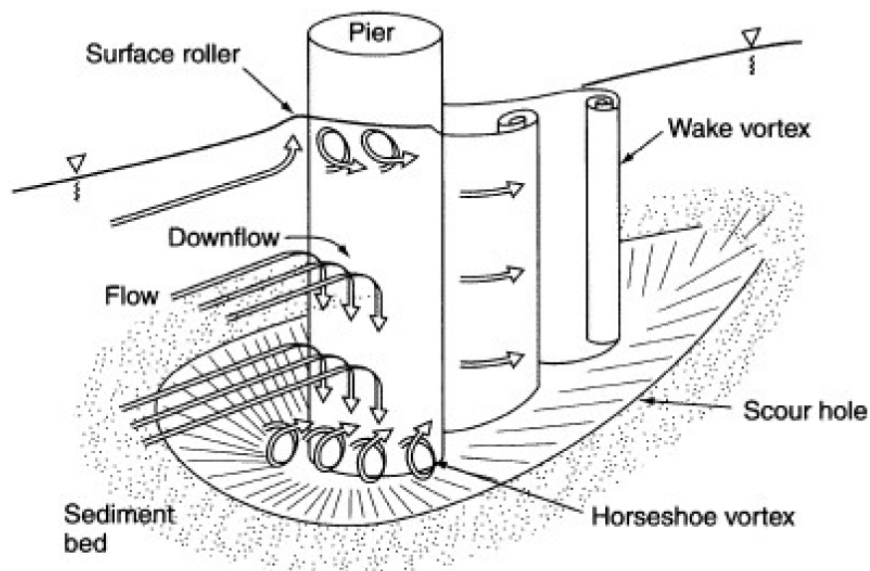
Figure 2.1: Formation of scour hole. Source: [9]

Figure 2.1 illustrates the mechanism of the formation of a scour hole.As flowing water approaches a structure (in this case, a monopile), the flow contracts and thus the velocity is increased. The flow is also forced into a

downflow motion in front of the structure. This motion gives rise to vortices (called the horseshoe vortex) at the seabed, which disturbs and transports the sediment away from the base of the monopile. Some scour is also seen due to vortex shedding at the leeward side of the monopile. In practice however, the major scouring occurs on the upstream side of piles through the horseshoe vortex mechanism [9]. This is also the reason why waves are not expected to contribute as substantially to scour - because the flow is not unidirectional. In fact, the back and forth wave action might disrupt the formation of the vortices, thus mitigating the impact of scour.

2.1.2. Time evolution of scour

Scour in the ocean is of the type live bed scour - meaning the inflow and outflow of sediments occurs simultaneously. Under current-dominated conditions, the scour is expected to eventually reach an equilibrium depth. This is the maximum depth of scour, as beyond this point the sediment flowing in is equal to the sediment flowing out. Several attempts have been made to predict this maximum scour depth - attempts have also been made to correlate this maximum scour depth to the metocean conditions of a given site [22]. Any design for scour protections etc., is generally based on this maximum depth.

However, a certain amount of uncertainty continues to exist as long as a model is based on a fixed maximum scour depth. Additionally:

- The flow regime in the ocean is capable of recompacting soil. Thus backfilling during evolution of scour is also important [33], as stiffness of backfilled soil may sometimes be even greater than the original soil.

- The ocean is not a current only regime. The combination of currents and waves ensures that the actual scour depth that is achieved is much lower than the current only situation.

Thus when the impact of scour is measured based on the assumption that a specific scour depth is seen over a long period of time, there is a substantial amount of uncertainty.

2.1.3. Impact of local and global scour

Scour can be either local (concentrated around the pile) or global (over the entire soil domain - for example, in a wind farm). Both types of scour alter the embedded depth and hence the lateral loading profile of a monopile.
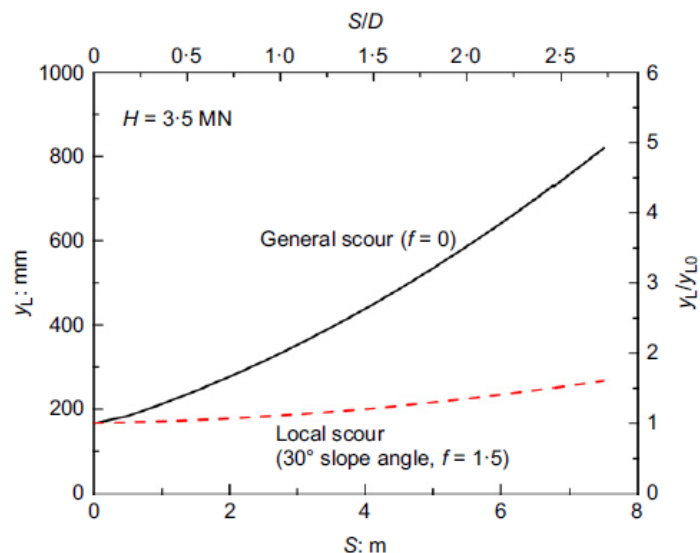
Figure 2.2: Scour-induced amplification of the lateral pile deflection. Source: [30]

In case of general scour, the lateral deflection is amplified much more than in case of local scour, as shown in figure 2.2. The local scour affects the p-y response (i.e., soil stiffness) at shallow depths - however, at a given depth below the scour base, stiffness is greater in case of local scour than global scour [30]. This shows the beneficial effect of the remaining overburden soil in case of local scour. Thus, modelling the shape of the scour hole accurately is valuable.

2.2. Performance of monopiles under scour

As mentioned previously, the lateral capacity and resonance frequency are the two primary parameters of a monopile affected under scour.

2.2.1. Eigenfrequency

It has been experimentally noted since some years that scour has significant impact on the resonant frequency of pile structures [28]. For offshore wind turbines specifically, experimental and numerical (EB beam with Winkler model) studies have illustrated a change in mode shape of the monopile due to scour (figure 2.3, 2.4) [29], [27].
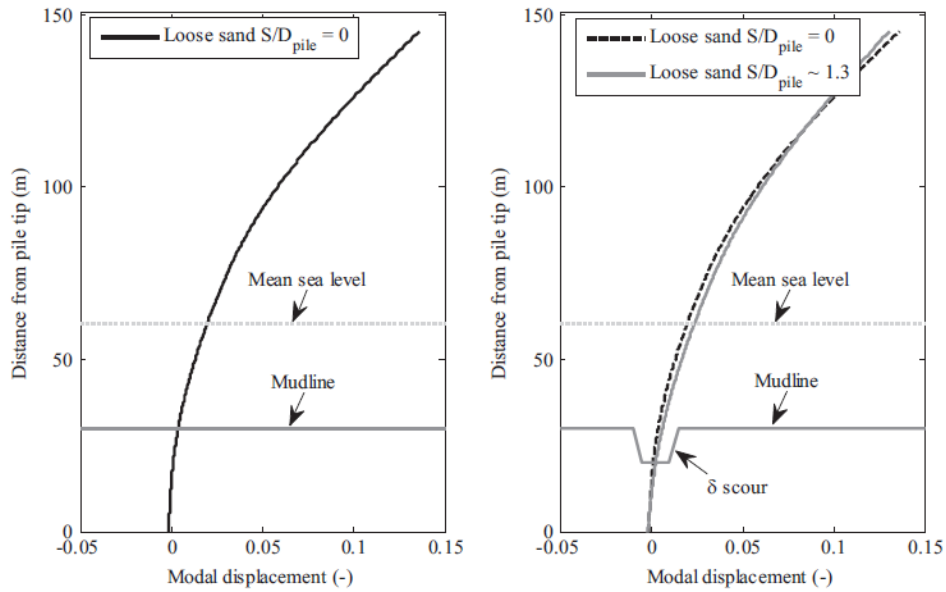
Figure 2.3: Change in mode shape for design scour ratio 1.3. Source: [29]
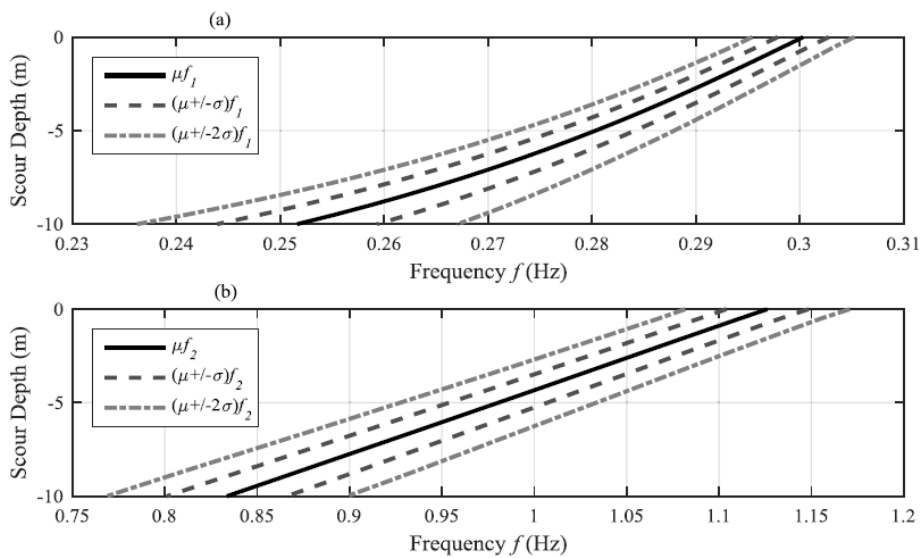
Figure 2.4: Mean and standard deviation of frequencies for different scour depth. (Top) First eigenfrequency (Bottom) Second eigenfrequency. Source: [27]

Despite spatial variability and geotechnical uncertainty, the changes due to scour are significant enough

that a correlation of scour depth to eigenfrequency alteration would be valuable [27].

2.2.2. Limit states and lateral capacity
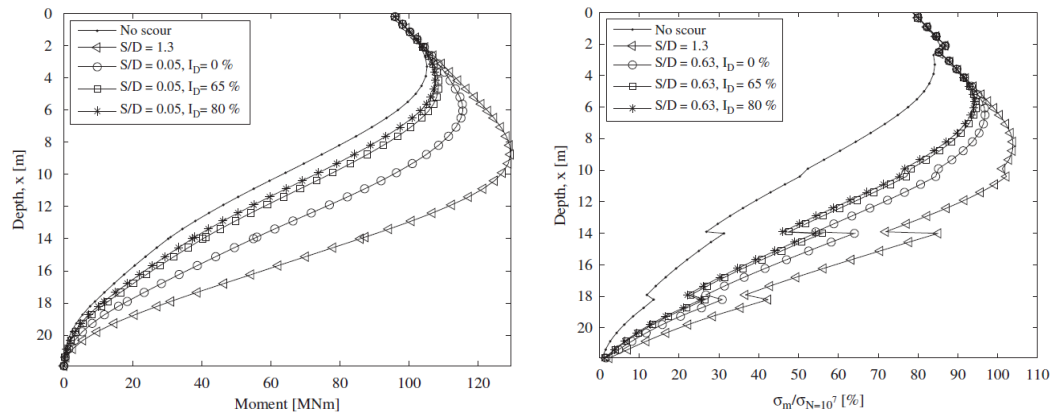
Figure 2.5: Limit state design of monopiles with and without scour. (L) Distribution of bending moment, M, under ULS-load for varying scour/backfilling conditions. (R) Variation with depth for the maximum cross-sectional stress relative to the fatigue capacity at N = 10^7 cycles for varying scour/backfilling conditions. Source: [33]

As shown in figure 2.5, the ULS and FLS design conditions for a monopile can vary significantly based on the exact scour conditions. The assumption of maximum scour depth is thus a highly conservative design. This is an important consideration in an industry like offshore wind, which is very sensitive to costs.

An FEM study of the lateral load capacity in PLAXIS shows significant reduction in lateral capacity with increase in scour depth [17]. As illustrated in figure 2.6, this corresponds to a reduction in lateral stiffness of the pile.
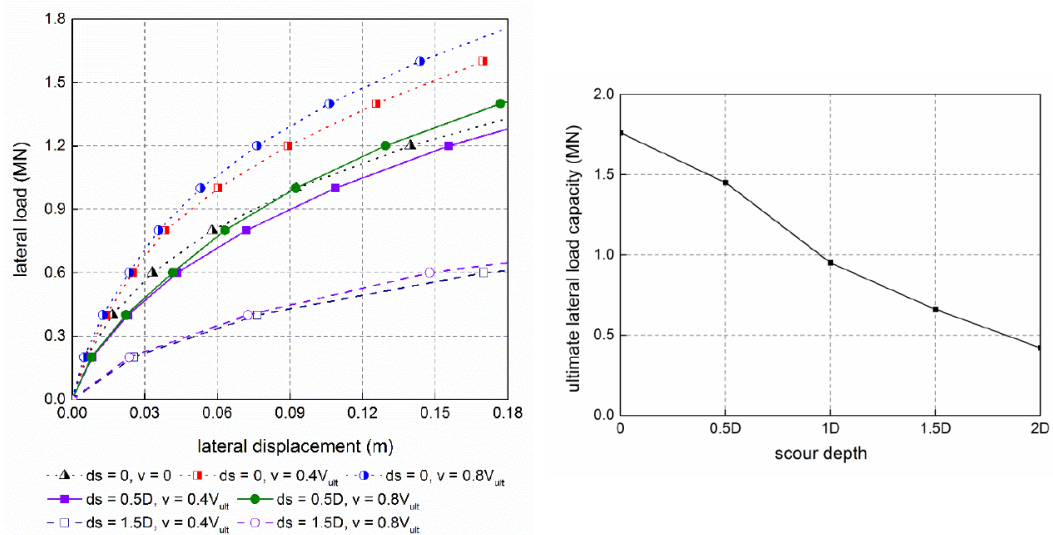
Figure 2.6: (L) Load displacement curves and (b) lateral stiffness of pile, for different scour depths. Source: [17]

2.3. Research Gaps

So far, the large section of studies on this subject have been experimental or have employed simplified numerical models like the Winkler model. Specifically, the study of the evolution of eigenfrequency with time, or a comp[arison between local and global scour, has not been done through full 3D Finite Element Method

simulation. As the soil stiffness and shape of scour hole has a substantial impact on the eigenfrequency of the turbine, it is expected that a full 3D FEM simulation would be valuable. Additionally, most of the literature mentioned above looks at monopiles with large L/D ratios. However with the manufacture of monopiles with large diameters of 8-10 m or more, the same studies may not apply. It is important to examine whether these larger, stiffer monopiles still show influence of scour upon their eigenfrequencies.

2.4. Aims and considerations for present study

A 3D soil model has recently been developed in OPENSEES for the purpose of frequency evaluation during storm conditions [15]. The model has the benefit of refined descriptions of soil-structure interfaces and HM coupling, while also allowing an examination of frequency over a given duration, as opposed to a fixed point in time (as is the case in previous studies). The model uses the u-p formulation to model the dynamic hydromechanical (HM) response, based on the assumptions of (a) small soil deformations, (b) incompressible soil grains, (c) solid and fluid phases with constant density and (d) negligible fluid acceleration [40]. The cyclic soil behaviour is modelled with the bounding surface plasticity model developed by Dafalias and Manzari [4] and the structure itself is modelled as a Timoshenko beam.

The aim of this study is to introduce scour into the above soil model and study its impact on an offshore wind turbine (OWT) system. Some considerations to be noted are:

- For the current period, it has been deemed most feasible to set scour only as an initial condition, as modelling time evolution of scour is an extensive task in itself.

- The initial scour shall be modelled for different depths. The dynamic response in the form of resonant frequency and damping effects can be evaluated.

- The study shall include local as well as global scour, for a conical scour hole with fixed slope angle.

- Loading shall be evaluated both for operating conditions and in the cut-off region. It is intended to use software generated loads as close to real world dynamics as possible.

- The effects of loading frequencies can also affect the dynamics. These impacts should be separated from the impact of scour.

With an advanced soil FEM model and realistic environmental loading, it is expected that the impacts produced by scour will be quite close to reality. The specific questions that are expected to be answered at the end of this study are:

- Whether scour has an impact on the resonant frequency of a turbine

- How the impact (if any) differs for local scour and global scour under different depths

- Whether non-linear soil is important for these examinations

- Whether scour has an impact on the damping of the OWT in non linear soil

The above questions are examined in the context of non-linear soil, for a large diameter monopile - both under operational and cut-off loading.

3

Integrated 3D Finite Element Model
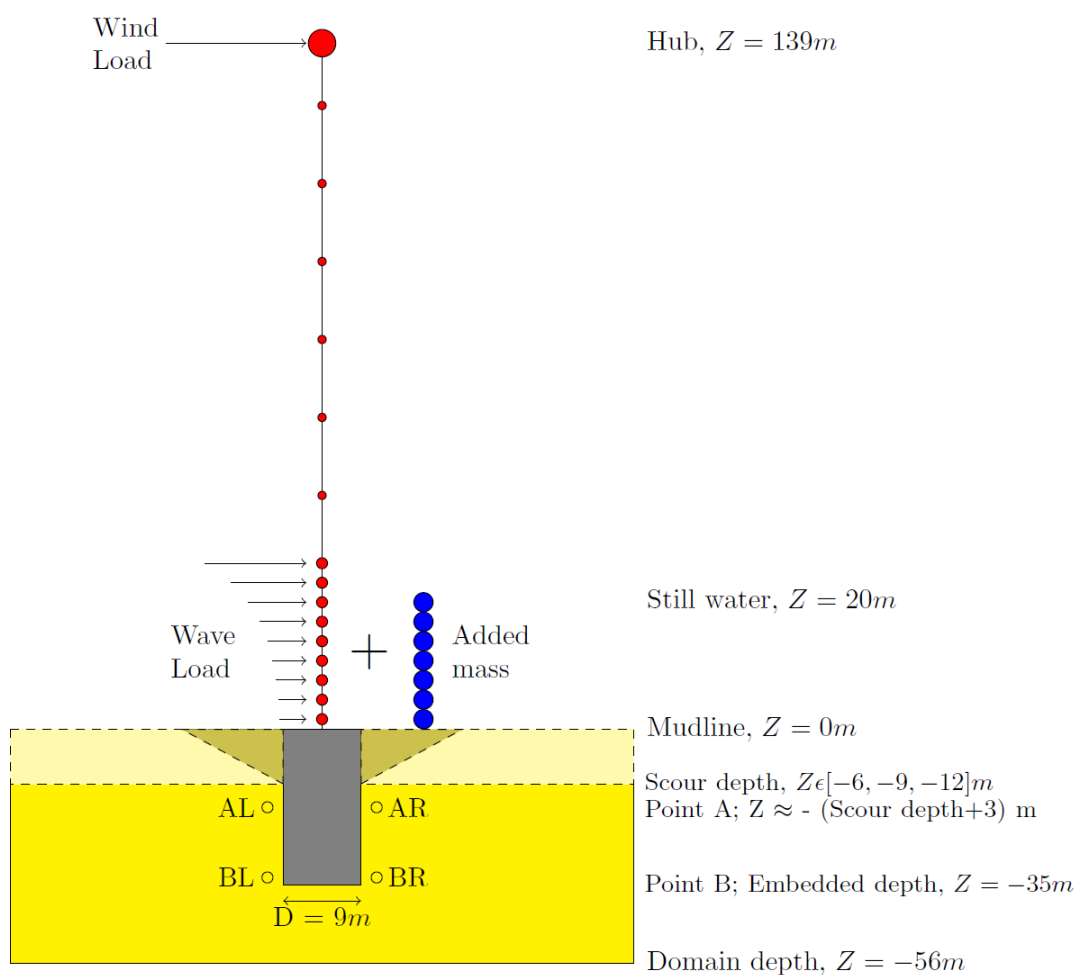
Figure 3.1: Schematic of the entire model (not to scale)

An integrated 3D FE model has been created, using the DTU 10 MW turbine and a suitable monopile, placed in sandy soil in 20 m deep water offshore. A schematic representation of the entire model is illustrated in figure 3.1.

The soil is Toyoura clean sand, with minor parameter modifications to match the soil used in monopile de-

sign. The nodes AL, AR, BL and BR in figure 3.1 represent the points at which soil is sampled to demonstrate soil behaviour as part of the results in section 4. The model is run for the following initial conditions:

- No scour

- Local scour 6 m (0.67D), 9 m (1D) and 12 m (1.33D)

- Global scour 6 m (0.67D), 9 m (1D) and 12 m (1.33D)

The dark yellow soil in the schematic represents the soil removed under local scour, whereas the light yellow area represents the additional soil removed under global scour. All models are subjected to operational loads, and some relevant ones are also subjected to storm loading at winds above cut-out velocity.

3.1. Wind turbine and monopile

The two most reliable, freely available turbine models in literature are the NREL 5MW turbine [12] and the DTU 10MW turbine [1]. However the current study aims to be relevant for the trends in the offshore wind industry, which is moving towards larger turbines - thus the DTU 10MW turbine is chosen for this analysis. The DTU 10MW tower is divided into 10 sections of varying thicknesses [1]. In the current model, the first section of this tower is further divided into pieces of 1 m length. This is for the ease of application of wave loads in case it is required. The remaining sections correspond to the sectioning of the DTU10MW turbine according to thickness changes. Thus, for each section, the thickness remains a constant and the other section properties like diameter, are taken as the mean of the initial and final values for each section. Furthermore, symmetry is applied and only half of the integrated soil-monopile system is modelled.

DTU 10 MW Turbine		
Rated speed	11.40	m/s
Cut in	4.00	m/s
Cut out	25	m/s
Tower mass	605000.00	kg
RNA mass	676000.00	kg
Hub height	119.00	m

Table 3.1: Wind turbine properties

Monopile		
Diameter	9.00	m
Thickness	0.11	m
Embedded depth	35.00	m
Interface height	20.00	m
Mass per unit length	24414.887	kg/m

Table 3.2: Monopile properties

Tower Properties	Bottom diameter	Top diameter	D scale	Thickness scale	Tower EI	Tower steel Poisson's ratio	Tower steel Density
	8.30 m	5.50 m	1.125	1.25	2.10E+11 Pa	0.30	8500.00 kg/m^3

Table 3.3: Tower properties

The complete table of tower section properties, as used in this thesis, is listed in the appendix. The RNA is modelled as a mass at the hub. The RNA mass and other properties of the DTU 10MW relevant to this study is listed in tables 3.1 and 3.3. The design of the monopile foundation, as well as some modifications to the tower properties, is in accordance with the design in [35]. The diameter, thickness and embedded depth for the 20 m water depth case is chosen - the relevant parameters are listed in table 3.2.

3.2. Soil structure interaction

The overall formulation of the soil model rests upon the study by Kementzetzidis et al [15]. In this model, the soil elements used are the H1-P1ssp bricks proposed by McGann et al [23]. The interaction between the pore water and soil skeleton is described using the u-p formulation developed by Zienkiewicz et al [40], and the cyclic soil behaviour is described using the consitutive model SANISAND04, as developed by Dafalias and Manzari [21].

3.2.1. Low frequency dynamics of saturated soils

The dynamic hydromechanical response of the soil is modelled with the $u-p$ formulation by Zienkiwicz et al [40], as mentioned above. This formulation is valid at low frequency dynamics of soil, where relative acceleration between the fluid and soil skeleton is negligible. Further, it also assumes that:

- The deformations in the soil are small

- The grains are incompressible

- Both solid and fluid phases have constant densities

- The fluid acceleration is negligible

The $u-p$ formulation is advantageous for the current offshore wind turbine applications as:

- Fluid acceleration is negligible in case of low loading frequencies [39] - a condition which is fulfilled for wind and wave loading with frequencies under 0.5 Hz, as is the case for this study.

- The $u-p$ formulation reduces the number of unknown variables per node relative to other finite element formulations - thus, the computational time and cost is reduced.

The $u-p$ formulation relies on the following governing equations:

$$\nabla.(\sigma' - p\mathbf{1}) + \rho\mathbf{g} - \rho\ddot{\mathbf{u}} = 0 \tag{3.1a}$$

$$\dot{\epsilon}_{vol} + \frac{n}{K_f}\dot{p} + \nabla.[\mathbf{k}(-\nabla p + \rho_f\mathbf{g})] = 0 \tag{3.1b}$$

This coupled set of equations represents the global equilibrium of the mixture (3.1a) and the mass balance of the fluid phase (3.1b). Equation 3.1b inherently includes the momentum balance as well as Darcy flow of the fluid. The symbols used denote the following:

- $\sigma', \mathbf{u}, \epsilon_{vol}, n$: effective stress, displacement, volumetric strain and porosity of the soil skeleton, respectively.

- ρ : Mass density of the mixture obtained as the porosity-weighted average of solid and fluid densities by the equation

$$\rho = (1-n)\rho_{\text{solid}} + (n)\rho_{\text{fluid}}$$

- K_f, ρ_f : Bulk modulus and mass density of the fluid

- $\mathbf{k}$ and $\mathbf{g} = [0,0,g]^T$: Permeability tensor and gravity acceleration field

- ∇ and $\nabla.$: Gradient and divergence operators

- $\dot{x}$: Time derivative of variable x

- $\mathbf{1} = [1,1,1,0,0,0]^T$: Vector representation of the Kronecker delta tensor

In the following study, the soil is assumed to have isotropic permeability. Thus a scalar value of k can be used as follows:

$$\mathbf{k} = k \begin{bmatrix} 1 & 0 & 0 \\ 0 & 1 & 0 \\ 0 & 0 & 1 \end{bmatrix}, \text{ where } k = \frac{k^{darcy}}{\rho_f g} \tag{3.2}$$

Thus the relationship between the scalar k and the Darcy permeability used as a standard in study of soil mechanics can also be seen.

Most of the above values are described as properties of the system. Of the unknowns, σ' and ϵ_{vol} are also dependent on the displacement field $\mathbf{u}$ - thus $\mathbf{u}$ and p are the only unknowns.

3.2.2. Finite element formulation

The weak form of the equation 3.1a and 3.1b are converted into a finite element system through the Galerkin-FE method with the proposed approximations of $\mathbf{u} \approx \mathbf{N_u d}$ and $p \approx \mathbf{N_p p}$ [38]. This leads to the system of equations 3.3, described below.

$$\overbrace{\vec{M}\vec{\ddot{d}}}^{\text{mixture inertiae}} + \overbrace{\int_{\Omega} \vec{B}^T \boldsymbol{\sigma}' d\Omega}^{\text{soil internal forces}} - \overbrace{\vec{Q}\vec{p}}^{\text{pore pressure forces}} = \overbrace{\vec{f}_{u,\Omega}^{ext} + \vec{f}_{u,\Gamma}^{ext}}^{\text{mixture external forces}} \tag{3.3a}$$

$$\overbrace{\vec{Q}^T\vec{\dot{d}}}^{\text{soil dilation/compaction}} + \overbrace{\vec{S}\vec{\dot{p}}}^{\text{fluid compressibility}} + \overbrace{\vec{H}\vec{p}}^{\text{seepage}} = \overbrace{\vec{f}_{p,\Gamma}^{ext} + \vec{f}_{p,\Omega}^{ext}}^{\text{fluid external fluxes}} \tag{3.3b}$$

where the relevant matrices/vectors are defined as:

$$\vec{M} = \overset{N_{el}}{\underset{m=1}{\mathbf{A}}} \left(\int_{\Omega^e} \vec{N}_u^T \rho \vec{N}_u d\Omega^e \right) : \text{mixture mass matrix} \tag{3.4a}$$

$$\vec{Q} = \overset{N_{el}}{\underset{m=1}{\mathbf{A}}} \left(\int_{\Omega^e} \vec{B}^T \vec{1} \vec{N}_p d\Omega^e \right) : \text{HM coupling matrix} \tag{3.4b}$$

$$\vec{S} = \overset{N_{el}}{\underset{m=1}{\mathbf{A}}} \left(\int_{\Omega^e} \vec{N}_p^T \frac{n}{K_f} \vec{N}_p d\Omega^e \right) : \text{fluid compressibility matrix} \tag{3.4c}$$

$$\vec{H} = \overset{N_{el}}{\underset{m=1}{\mathbf{A}}} \left(\int_{\Omega^e} \nabla \vec{N}_p^T \vec{k} \vec{\nabla} \vec{N}_p d\Omega^e \right) : \text{permeability matrix} \tag{3.4d}$$

$$\vec{f}_u^{ext} = \vec{f}_{u,\Omega}^{ext} + \vec{f}_{u,\Gamma}^{ext} = \overset{N_{el}}{\underset{m=1}{\mathbf{A}}} \left(\int_{\Omega^e} \vec{N}_u^T \rho \vec{g} d\Omega^e \right) + \overset{N_{el}}{\underset{m=1}{\mathbf{A}}} \left(\int_{\Gamma^e} \vec{N}_u^T \vec{t} d\Gamma^e \right) : \text{mixture external force vector} \tag{3.4e}$$

$$\vec{f}_p^{ext} = \vec{f}_{p,\Omega}^{ext} + \vec{f}_{p,\Gamma}^{ext} = - \overset{N_{el}}{\underset{m=1}{\mathbf{A}}} \left(\int_{\Omega^e} \nabla \vec{N}_p^T \rho_f \vec{k} \vec{g} d\Omega^e \right) + \overset{N_{el}}{\underset{m=1}{\mathbf{A}}} \left(\int_{\Gamma^e} \vec{N}_p^T \vec{q} d\Gamma^e \right) : \text{fluid external flux vector} \tag{3.4f}$$

This finite element system is implemented in OPENSEES with the SSPbrickUP element. These elements consist of low order, eight-noded, hexahedral bricks. They employ a stabilization scheme which allows single point integration for the soil elements, and avoids spurious checkerboard pore pressure modes. The elements specifically show good performance near the undrained-incompressible limit, and have the following additonal features:

- enhanced assumed strain field to handle volumetric and shear locking

- analytical pre-integration for the solid phase response stabilization, which makes it computationally more efficient

- $\mathbf{N_u}$ and $\mathbf{N_p}$ as linear interpolation function

- non-residual based stabilization scheme to handle dynamic HM response in undrained/incompressible cases

The non-residual based stabilization scheme, however, adds a laplacian term to equation 3.3a:

$$\vec{Q}^T\vec{\dot{d}} + \left(S + \tilde{H} \right) \vec{p} + \vec{H}\vec{p} = \vec{f}_{p,\Gamma}^{ext} + \vec{f}_{p,\Omega}^{ext}, \quad \text{where:} \quad \vec{\tilde{H}} = \overset{N_{el}}{\underset{m=1}{\mathbf{A}}} \left(\int_{\Omega^e} \nabla \vec{N}_p^T \alpha \vec{\nabla} \vec{N}_p d\Omega^e \right) \tag{3.5}$$

The α parameter injects a pseudo-stabilization into the pore pressure field. However too low or too high α values may result in ineffective or excessive stabilisation. The range of α used in this study is given by equation **??** [11].

$$\alpha = \frac{\alpha_0 h_{el}^2}{G_s + \frac{4}{3} K_s} \tag{3.6}$$

Here, h_{el} is the average element size of the mesh, and G_s and K_s are the bulk and shear moduli of the sil skeleton. Based on average element size, this parameter is set in the order of 10^{-6}. The permeability throughout the soil domain is assumed to be uniform, in the order of $k = 10^{-5}$ m^3/day.

The final model implemented in OPENSEES was developed in the University of Washington [8]. The details of the code can be found online at [26].

3.2.3. Constitutive modelling of cyclic soil behaviour

The cyclic soil behaviour is described using the bounding surface plasticity model developed by Dafalias and Manzari [21]. The modifications by the authors in 2004 to account for fabric changes under dilatancy [4], as well as the proposals by Liu et al to counter for ratcheting phenomena [18],[19], are also included. The main features of the implemented constitutive model are as follows:

- The formulation is controlled by the stress ratio $\mathbf{r} = \frac{\mathbf{s}}{p} = \frac{\text{Deviatoric}}{\text{Hydrostatic}}$, with no presence of hydrostatic yield loci, like [36].

- back stress ratio (α) is used to formulate kinematic hardening

- an independent of J_3 deviatoric stress invariant, very small in size and circular on the π plane yield surface;

- the critical state parameter ψ is used to account for effective confinement stress levels and void ratio effects

- bounding surface M^b, which allows to model the softening response of dense samples but also reverse and cyclic modelling response simulation by moving into stress space as a function of ψ;

- phase transformation surface M^d which helps distinguish dilative and compactive soil response, and moves in stress space with reference to the critical state line M according to ψ;

- a stress ratio related hardening modulus which depends on the distance of back stress ratio tensor α, and the back stress ratio of the projection of the normal to the yield surface upon the bounding surface $\alpha_\theta^{\mathbf{b}}$, to model softening response

- a fabric dilatancy tensor $\mathbf{z}$ which allows for enhanced contractile response upon reversal of loading after a loading phase which induces dilatancy , due to changes in the fabric of non-cohesive soils
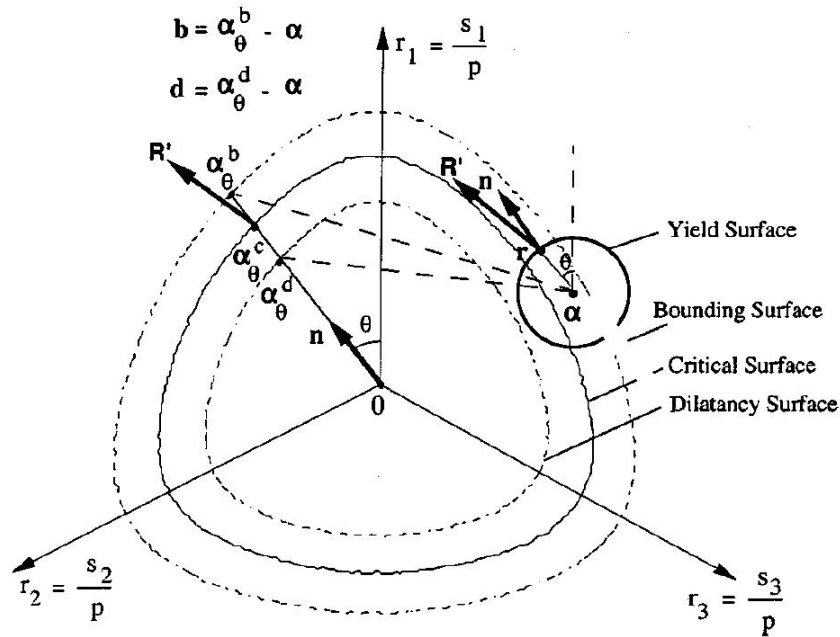
Figure 3.2: Schematic of yield, critical, dilatancy, and bounding surfaces on the stress ratio π plane. Source: [4]

3.2.4. Final calibration

Similar to [15], this study also inserts a weaker or degraded interface sand layer along the shaft of the monopile and under the tip. This layer is intended to replicate friction fatigue effects in the real world soil. A set of 15 soil parameters is used for its calibration. The final soil parameters used in the model are listed in table 3.4.

This calibration uses the calibration for Toyoura clean sand with 80% relative density, largely drawing upon the original parameters in [4], but with modifications to void ratio to match [35] as described below. Some further alterations are also made for the degraded sand at the pile-soil interface, and the strengthened soil on the scour slope.

Variable		Value		
		Toyoura Sand	**Pile-Soil Interface**	**Exposed Scour Slope**
Elasticity	G_0	125	100	150
	ν	0.05	0.05	0.05
Critical state	M	1.25	1.00	1.50
	c	0.712	0.712	0.712
	λ_c	0.019	0.019	0.019
	e_0	0.715	0.715	0.715
	ξ	0.7	0.7	0.7
Yield surface	m	0.01	0.01	0.01
Plastic modulus	h_0	7.05	7.05	7.05
	c_h	0.968	0.968	0.968
	n^b	1.1	1.1	1.9
Dilatancy	A_0	0.704	0.704	0.704
	n^d	3.5	3.5	3.5
Fabric-dilatancy tensor	z_{max}	4	4	4
	c_z	600	600	600

Table 3.4: Parameters for soil calibration at pile-soil interface, on slope of scour and in the remaining soil domain

In addition to the above however, it is important to maintain some consistency with the soil model used in [35] so that the monopile design remains valid. As the monopile design is based on the drained strength of soil, it is assumed that the matching of the internal friction angle of the Toyoura sand in [15] to the HS sand in [35] would be sufficient for the monopile design to remain valid.
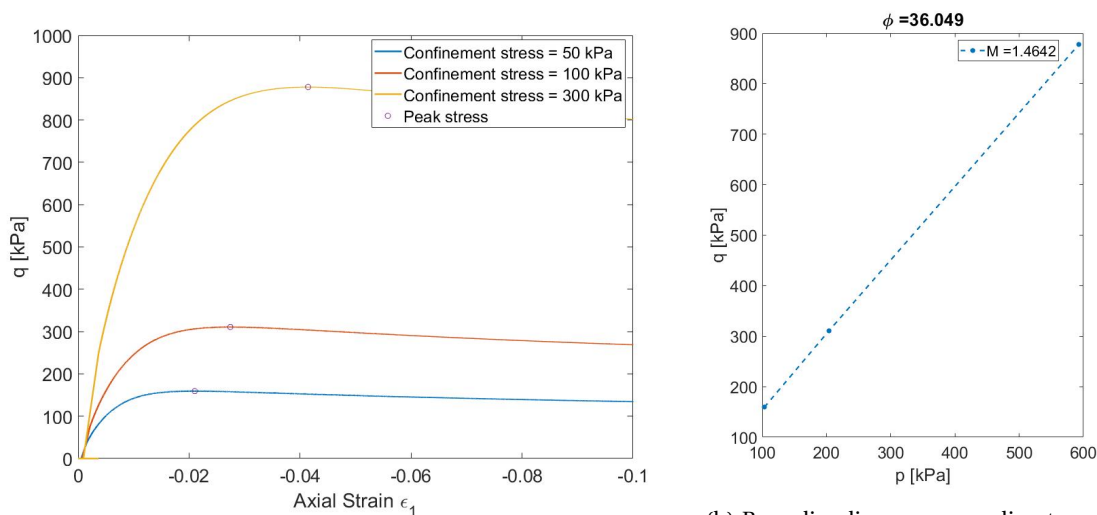
(a) Soil reponse in triaxial test, with markers for peak stress points

(b) Bounding line corresponding to peak stress, with M = 1.4643 and $\phi = 36°$

Figure 3.3: Results of triaxial test on sand corresponding to void ratio of 0.715

The Manzari Dafalias model is quite sensitive to void ratio changes. The sample Toyoura sand from [15] is subjected to a set of drained triaxial compression test with confining stresses of $50kPa$, $100kPa$ and $300kPa$.

The void ratio is modified by trial and error until the peak stress values from the triaxial test correspond to a line of slope $M = 1.43$. Applying this to the HS sand model, the internal friction angle ϕ can be calculated from the equation 3.7 as 36.049°.

$$M = \frac{6\sin\phi}{3 - \sin\phi} \tag{3.7}$$

This sufficiently matches the internal friction angle of 36° used in [35]. The slope $M = 1.46$ is found to correspond to a void ratio of 0.713. The corresponding triaxial test results are shown in figure 3.3.

3.3. Scour conditions

Scour is added as an initial condition to the respective models. The scour depths used are 6 m, 9 m and 12 m respectively, corresponding roughly to 0.7D, 1D and 1.3D, respectively. 1.3D is considered the equilibrium scour depth in a majority of cases by the design codes [5]. In case of local scour, a conical hole of bottom radius equal to the outer radius of the monopile and top radius corresponding to slope angle 15.76°, is added to the model. In case of global scour, the entire seabed is approximated to have lowered, although the other conditions remain similar to local scour.

As modelling of scour hydrodynamics is in itself a very extensive task, the scour is entered as an initial condition which remains unchanged during the simulation. In order to maintain a stable unsupported slope for this duration, the following modifications have been made:

- The slope angle is very low, at 15.76°.

- The exposed elements on the slope are modelled as a stronger layer of soil, with 20% increase in G_0 and M_c parameters, and a corresponding 10% decrease in initial void ratio.

- The bounding surface of these exposed elements is extended by increasing n^b to 1.9.

- The tolerance factors of these elements is 50 times higher than all other soil elements.

Due to the modification, the layer of exposed elements on the slope do not accurately represent soil behaviour. However, as this is a thin layer with a small number of elements, with minimum contact with the monopile, their impact on the important areas of soil behaviour is expected to be negligible. On the other hand, these modifications are highly beneficial in maintaining slope stability, which is essential to completing the study.

3.4. Environmental loading

Two types of environmental loading are applied to the integrated FE models. One in the operational region of the wind turbine, and the other a case of extreme loading beyond cut-out velocity of the turbine. In all cases, the initial 100s period is used as a ramp which builds up to the actual loading, to avoid effects of sudden change in loading. This is followed by 600s of the actual environmental loading. In case of the higher environmental load, there is an additional 100s at the end where the loading is 'switched off', allowing examination of the damping ratio of the sand.

Load Condition	Region	Mean V_{wind} [m/s]	Turbulence model	Water depth [m]	T_p [s]	H_s [m]	Wave spectrum
env1	Operational	12.6	NTM	20	6.5	1.25	Pierson-Moskowitz
env2	Parked	25	NTM	20	12.0	6.0	JONSWAP

Table 3.5: Parameters for applied environmental loading

3.4.1. Aerodynamic loading

The aerodynamic loading at the hub is generated by the software SIMA, developed by SINTEF Ocean (formerly MARINTEK) [13]. This software is primarily intended for coupled aero-hydro-servo-elastic simulations of offshore wind turbines. For this study, the software is used in limited capacity, to obtain the environmental loading on the DTU 10MW turbine. The foundation and other specifications are in accordance with [35].

The normal turbulence model (NTM) [3] is used to generate turbulent wind loading at the hub for mean wind

speeds of 12.6 m/s and 25 m/s, respectively. The loads are generated with the nacelle fixed in space, and a damper is later added to the hub of the OpenSees model to represent aerodynamic damping due to operation of the turbine. The damping ratio used for this purpose is 6%, based on the study by Hegseth and Bachynski [10].

When applying the load in OPENSEES, an initial ramp of 100s is added in order to avoid transient effects and instability. There is a gradual linear increase in F_{mean}, as well as an exponential increase in the amplitude of loading, during this time period. The final wind load as applied to the model is shown in figure 3.4.
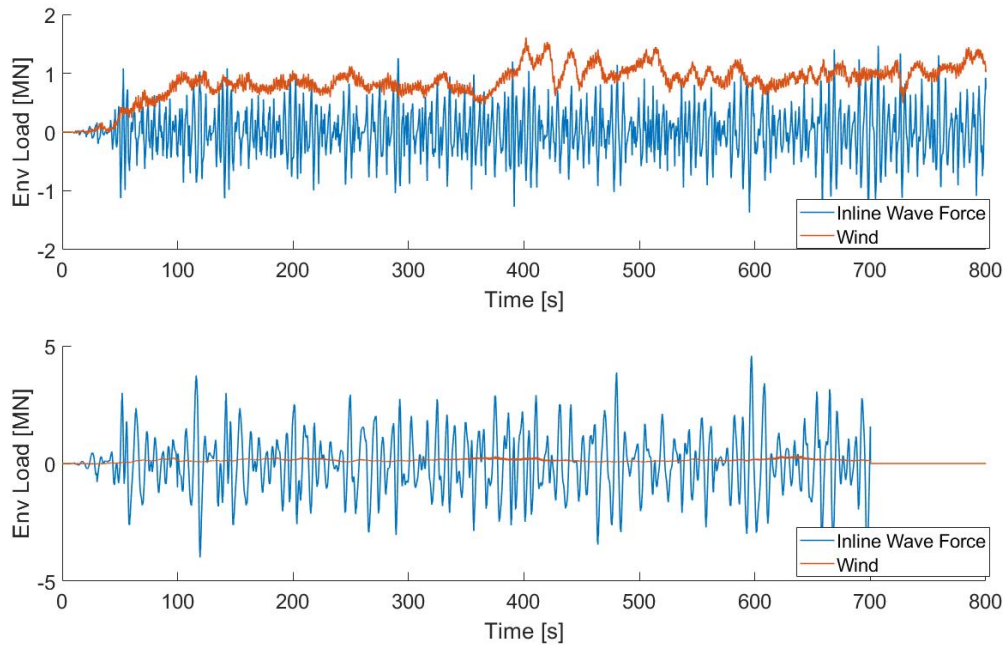
Figure 3.4: Applied environmental loading under operational (top) and storm (bottom) conditions

3.4.2. Hydrodynamic loading

The software SIMA is used to generate the irregular wave kinematics at all necessary nodes. The significant wave height (H_s) and peak period (T_p) are according to the conditions in table 3.5. Wave kinematics is generated for all nodes from the seabed, up to 25 m height from the seabed. Of this, the first 20 nodes (up to still water level) are on the monopile, and the next 5 nodes are the first 5 nodes of the wind turbine. Each node corresponds to an element of 1 m length.

Once the wave kinematics (specifically velocity and acceleration) are generated, the Morison equation as shown in 3.8 ([24]) is used to calculate the wave force at each node. The equations are calculations for a span length of $1m$ and the resulting load is applied to a single node within the span. The sum of the wave forcing at all nodes is the inline wave force. Due to the large diameter of the pile, the MacCamy Fuchs correction should be applied [20]. However, for operational loads, C_M is still found to be around 2.0, and in case of storm loading, diffraction is negligible.

$$F_{\text{Hyd}} = F_{\text{drag}} + F_{\text{inertia}} = \frac{1}{2}\rho C_D D |U|U + \rho C_M A \frac{dU}{dt} \tag{3.8}$$

The inline wave force is shown in figure 3.4. In case of the applied wave forcing, a 100s ramp is also introduced, during which the wave amplitude increases gradually.

Under scour conditions, it is expected that the hydrodynamic loading will vary slightly. In the only literature found on the subject [2], Christensen et. al suggest that hydrodynamic forces do exist within the scour hole, but a full 3D CFD simulation would be required to properly assess the exact loading. In the present work, the loading at the lowest node of the monopile above seabed is simply extruded as a uniform load applied to each node within the scour hole.

3.5. Algorithms for analysis

Time marching refers to update of the known values of all relevant variables at time t_n, over one step increment δt to time t_{n+1}. Here the Newmark method ([25]) is employed with $\beta = 0.6$ and $\gamma = (\beta + \frac{1}{2})^2 = 0.3025$, which gives an unconditionally stable time integration. The accelerated Krylov Newton algorithm ([31]) is used to obtain the iterative solution at each step increment. For the non-linear soil constitutive model, the forward Euler explicit algorithm ([32]) is used to integrate and update the soil stresses, strains and hardening variables over the step increment.

3.6. Stockwell transforms

The usual frequency analysis of an OWT system involves a Fourier transform of hub displacement, which shows the frequency content of the collected motion over entire time history. This approach does not allow for capture of the change in frequency over time, and shifts in dominant frequency over time only contributes to a more noisy spectrum.

The time resolution can be tackled by short term Fourier transform, which applies the Fourier transform to a moving time window on the signal. However, this results in good resolution in the frequency domain, but rather poor resolution of the time domain. Wavelet transforms on the other hand, use wavelets (wave-like oscillations but with a finite duration fixed in time and space) that allow for better time resolution. The Stockwell transform or S-transform - utilized in this study - is an extension of the continuous wavelet transform which is based on a shifting Gaussian window in time, thus providing better frequency and time resolution than either method above.

$$S(\tau, f) = \int_{-\infty}^{\infty} u(t) w(t - \tau, f) e^{-2i\pi f t} dt \tag{3.9}$$

The Gaussian window employed is as follows:

$$w(\tau, f) = \frac{|f|}{k\sqrt{2\pi}} e^{-\frac{f^2 t^2}{2k^2}} \tag{3.10}$$

Here, f is the frequency, t is time, τ is the time at which the window is fixed and k is a variable which controls how many oscillations there are in a single window. A higher value of k results in poorer time resolution, but a lower value results in poorer frequency resolution. Thus a trade-off is required. For this study, a value of $k = 0.8$ is used.

3.7. Space discretisation

The meshing of the model is decided through a mesh sensitivity analysis found in appendix A. The final selected meshes are shown in figures 3.5, 3.6 and 3.7.
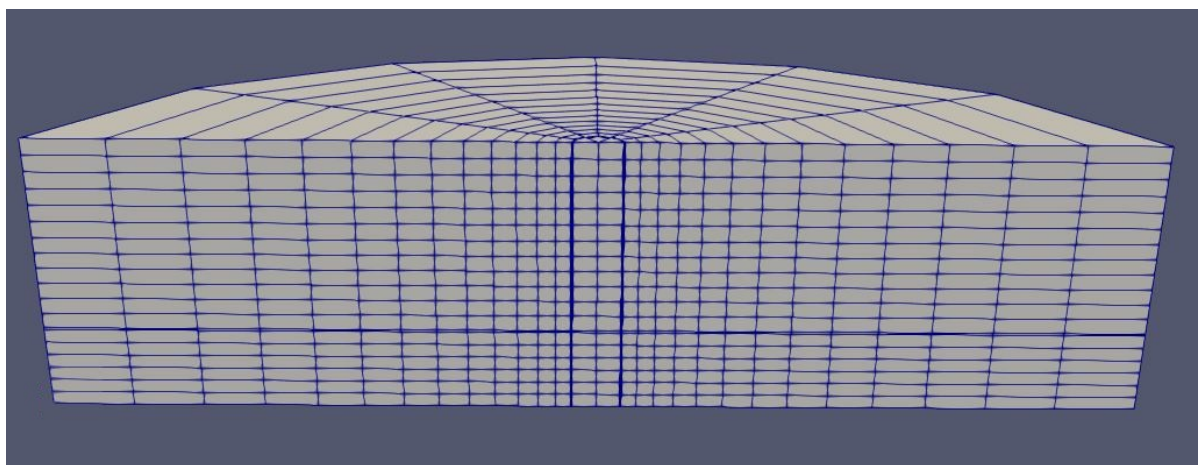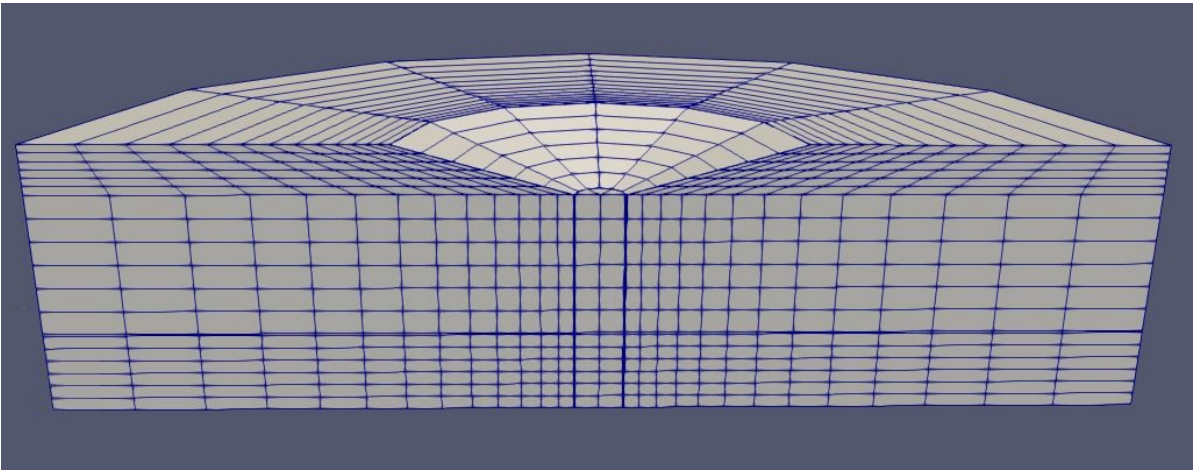

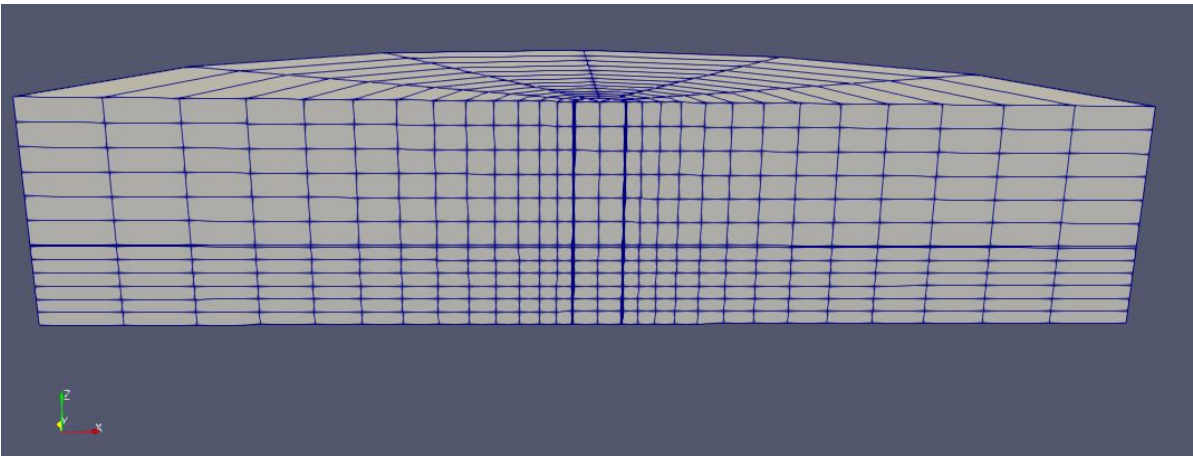Figure 3.5: Mesh for no scour condition

Figure 3.6: Mesh for 1D local scour

Figure 3.7: Mesh for 1D global scour

4

Non-linear performance under scour

In order to evaluate non-linear performance of the turbine under scour, the following scour models are examined:

- No scour

- 0.67D (or 6 m) global scour

- 0.67D (or 6 m) local scour

- 1.0D (or 9 m) global scour

- 1.0D (or 9 m) local scour

- 1.33D (or 12 m) global scour

- 1.33D (or 12 m) local scour

The performance of the models is evaluated by examining the s-transform and power spectrum of hub displacement, as well as the damping under impulse and under a rotor stop experiment under extreme loads. In addition, the development of pore water pressure for quasi-drained and undrained situations is also examined.

Table 4.1: Dominant response frequency under enviromental loading

Scour condition	Operational Load			Cutoff Load		
	Global [Hz]	Local [Hz]	Cantilever [Hz]	Global [Hz]	Local [Hz]	Cantilever [Hz]
No scour	0.2918	0.2918	0.3100	0.2999	0.2992	0.3100
0.67D	0.2825	0.2866	0.3037	0.2941	0.2999	0.3037
1D	0.2710	0.2810	0.3007	0.2706	0.2934	0.3000
1.33D	0.2643	0.2725	0.2970	0.2641	0.2861	0.2963

Table 4.2: Dominant response frequency under impulse loading

Scour Depth	Linear Elastic, 1MN		Non linear, 1 kN		Non linear, 1MN		Non linear, 9MN	
	Local [Hz]	Global [Hz]	Local [Hz]	Global [Hz]	Local [Hz]	Global [Hz]	Local [Hz]	Global[Hz]
No Scour	0.3010	0.3010	0.3010	0.3010	0.2936	0.2936	0.2852	0.2852
0.67D	0.2960	0.2960	0.2995	0.296537	0.2926	0.2847	0.2798	0.2758
1.00D	0.2926	0.2921	0.2980	0.292596	0.2882	0.2763	0.2739	0.2675
1.33D	0.2877	0.2862	0.2960	0.287671	0.2813	0.2650	0.2650	0.2586

Table 4.3: Evaluated damping ratios [%]

Scour Depth	Linear Elastic, 1MN		Non linear, 1 kN		Non linear, 1MN		Non linear, 9MN	
	Local	Global	Local	Global	Local	Global	Local	Global
No Scour	0.439	0.439	0.530	0.530	0.773	0.773	2.457	2.457
0.67D	0.425	0.426	0.229	0.163	0.865	1.323	2.739	3.351
1.00D	0.420	0.424	0.270	0.208	1.129	1.891	3.274	4.144
1.33D	0.423	0.422	0.125	0.663	1.573	2.624	4.787	5.410

The models are also compared to corresponding fixed based cantilever models as a reference, with the Timoshenko beam of the corresponding models being fully fixed at scour depth (or mudline, in case of no scour). All resulting numbers are tabulated in tables 4.1, 4.2 and 4.3, and salient observations are noted below.

4.1. Fixed base cantilever

A very simple representation of a wind turbine under scour is a cantilever fixed at the mudline (or scour depth, respectively). A mass is added to the free end of the cantilever to represent the RNA mass. The scour in this scenario is represented by the increasing length of cantilever. Upon examining this model under impulse and environmental loads, it is seen that there are small drops in the resonance frequency due to the increased length (table **??**). A sample comparison for the operational load case is in figure 4.1.

Table 4.4: Resonance frequencies of fixed base cantilever

Model	Resonance Frequency [Hz]			Normalized w.r.t. no scour condition		
	Impulse	Operational	Cutoff	Impulse	Operational	Cutoff
No Scour	0.3107	0.3100	0.3100	1.000	1.000	1.000
0.67D	0.3043	0.3037	0.3037	0.979	0.980	0.980
1.00D	0.3008	0.3007	0.3000	0.968	0.970	0.968
1.33D	0.2974	0.2970	0.2963	0.957	0.958	0.956

However this change is quite small (less than 4.5% even for the maximum scour depth), relative to the much larger drop (up to 11%, refer table 4.7) seen upon defining a soil model. Additionally, the resonance frequency in the cantilever case is consistently much higher than that of a model with more realistic representation of the soil (figure 4.5). The difference in frequency due to forcing also becomes apparent only at high scour depths (1D and 1.33D).

Hence, it is inferred that a study based on the fixed base cantilever model is insufficient to predict effects of scour.
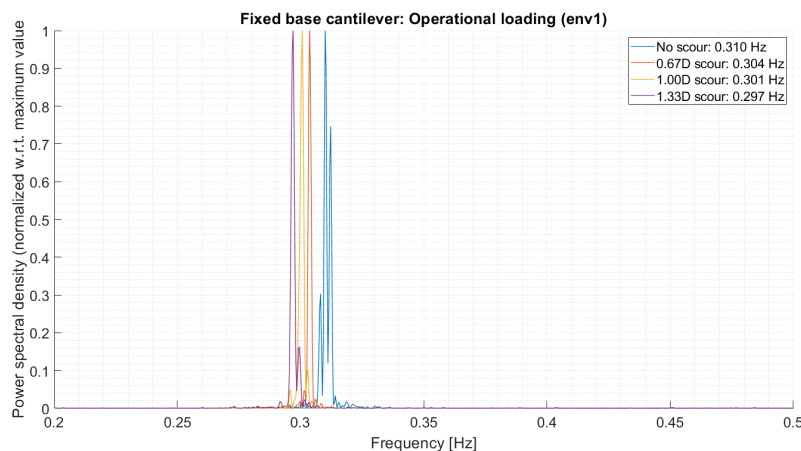

Figure 4.1: Normalized power spectral density of hub displacement for operational loading: no scour, local 1D scour and global 1D scour cases

4.2. Examination of 1D scour case

4.2.1. Hub displacement

While global displacements oscillate about a zero mean value under impulse loading, the both types of environmental loading shows a clear difference between no scour, global scour and local scour cases. The displacements seem to follow the dominant load pattern quite closely. This is seen specifically in case of the operational load, by comparing displacements in figure 4.3 to the dominant loading (i.e., the aerodynamic loading) of figure 3.4. The displacement response across no scour, global scour and local scour seems to conform to a similar pattern, but with a displaced mean. The mean displacement for global scour is consistently higher. The mean displacement for local scour is the next highest, but the gap between global scour and local scour is generally much higher than that between local and no scour.
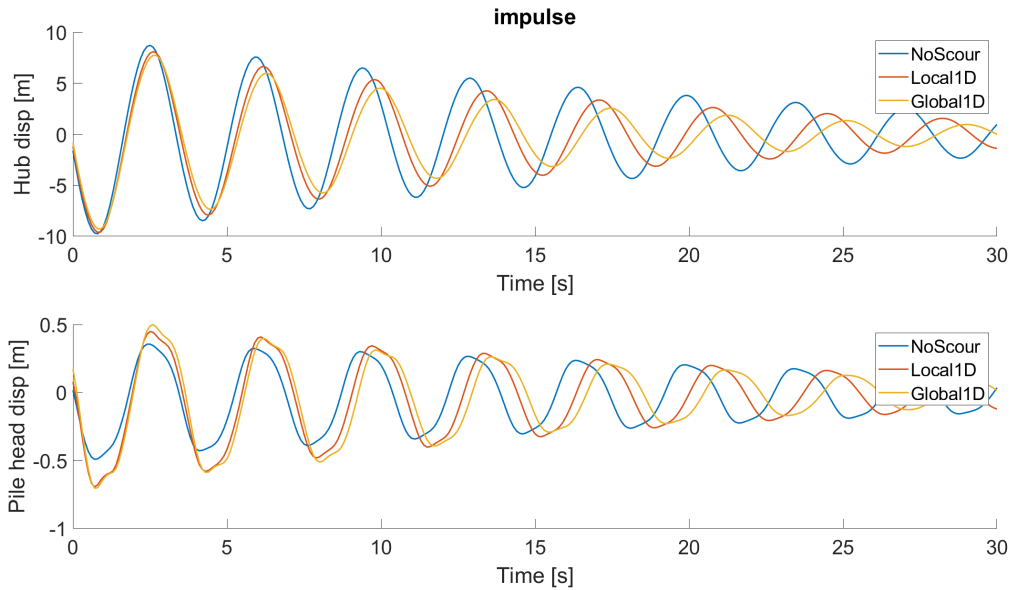

Figure 4.2: Hub displacement and pile head displacement for impulse loading: no scour, local 1D scour and global 1D scour cases
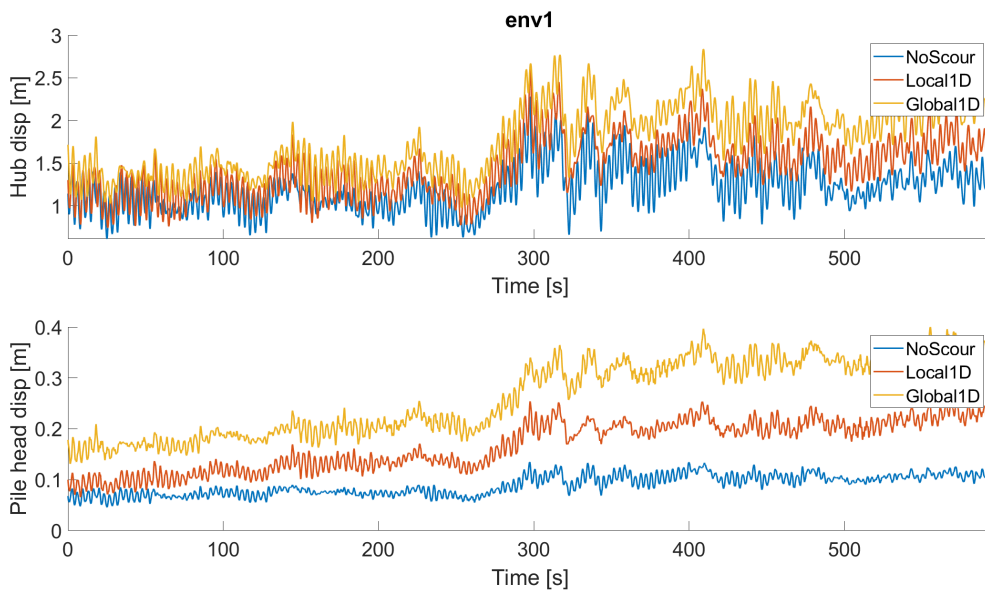

Figure 4.3: Hub displacement and pile head displacement for operational loading: no scour, local 1D scour and global 1D scour cases
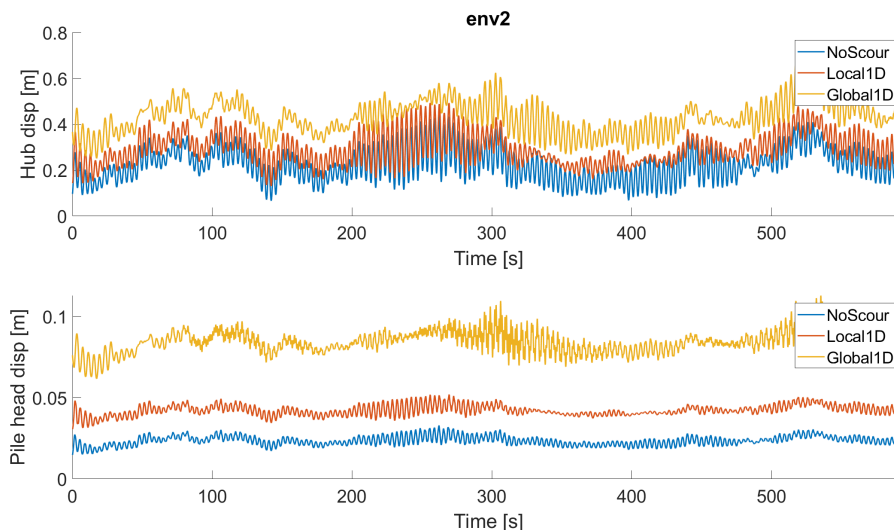
Figure 4.4: Hub displacement and pile head displacement for cutoff loading: no scour, local 1D scour and global 1D scour cases

This consistent trend can be understood by noting the resistance to movement around the bottom of the OWT for each case. The no scour case offers the least scope for the pile to displace below mudline, while the global scour offers the maximum scope. Thus the embedded depth of the pile is considerably increased for global scour relative to the no scour case, with the local scour case falling somewhere in between. The smaller the excavation for local scour, the closer it should be to no scour relative to global scour. Hence, as the scour depth (and thus also the radius) increases, the mean displacement of local scour is expected to move closer to the global scour case.

In case of hub displacement, the responses are too close to discern such a variation, but in case of pile head displacement, it is easier to note the trend. The mean displacement in all scour cases, and the relative position of local scour with respect to the midpoint between mean global scour and mean no scour displacement, is shown in table 4.5. As is evident from the % difference, the mean displacement under local scour increases from being closer to no scour condition, up to the midpoint between mean global and no scour displacements. With a large enough scour depth, it is expected that the local scour displacement will approach the global scour values.

Table 4.5: Relative position of pile head displacement under local scour with respect to global and no scour

Model	Mean pile head displacement [m]		Midpoint between global and no scour [m]	% decrease of local scour w.r.t. midpoint
	Global	Local		
No Scour	0.0930	0.0930	NA	NA
0.67D	0.1875	0.1074	0.7129	5.6369
1.0D	0.2807	0.1787	0.7595	3.2506
1.33D	0.3888	0.2322	0.8135	2.5042

4.2.2. Resonant response frequency

In the fixed base cantilever model, the scour being represented by the length of cantilever implies that there is no difference between global and local scour representation. In the full model, similar trends are seen where scour causes a drop in frequency, but there is a distinctive difference between global and local scour which is noted 4.5. The global scour causes the larger drop in natural frequency, relative to no scour condition. The trends in resonance frequency for local vs global scour across all the scour depths is discussed further in the next section. All frequencies show a large drop with respect to the fixed base cantilever.
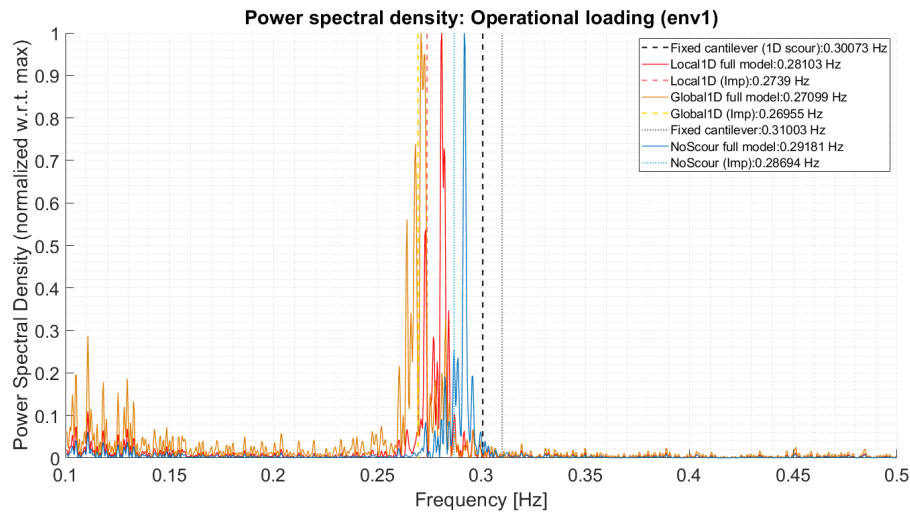
Figure 4.5: Normalized power spectral density of hub displacement for operational loading: no scour, local 1D scour and global 1D scour cases

Additionally, it may be noted that the global scour has the lowest percentage of energy associated with its dominant bending mode, as can be observed from the heights of peaks at other frequencies in figure 4.5. To help explain this, the S-transforms of the three cases are illustrated in figures 4.6, 4.7 and 4.8 below.

As is clear from these S-transforms, the dominant response frequency does not correspond to the first mode resonance frequency of the OWT throughout the simulation. At several points, the frequency drops to the vicinity of about $0.1 Hz$, which is where the loading frequencies are expected to lie. Thus it can be concluded that the energy of vibration is divided between the loading frequencies and the OWT's natural modes - and on occasion, the loading frequencies become dominant in the vibration of the tower. It is important to remember this as OWT design is generally done assuming that the resonance frequency of the system is dominant - but evidently, the loading frequencies can often become dominant as well.

The effect is minimum in case of no scour condition, but increases with local scour, and then maximum impact of loading frequencies is seen in the global scour cases. In case of higher scour depth, it is likely that the loading frequencies become dominant for large stretches of time.
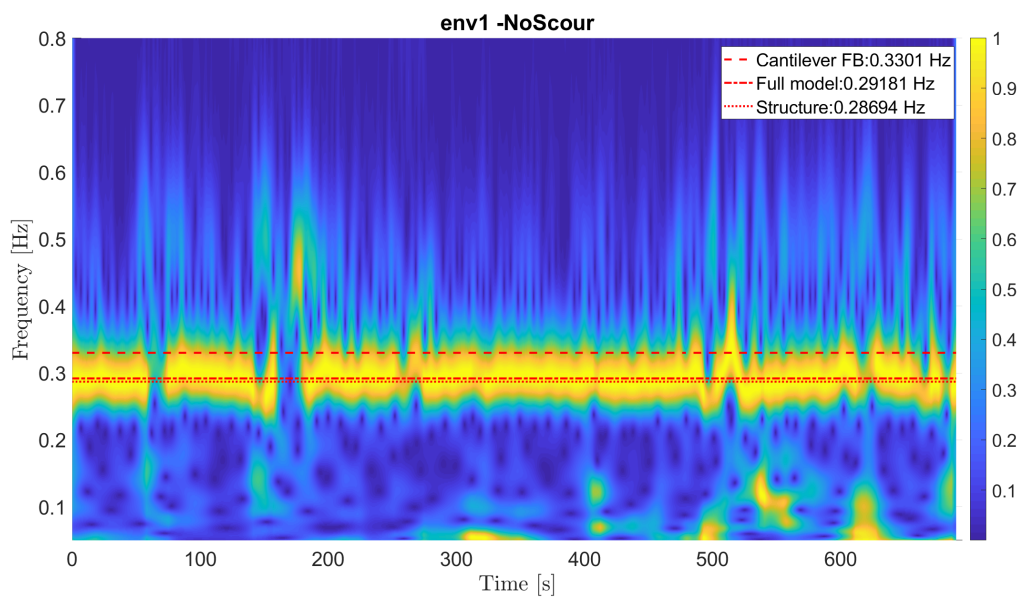

Figure 4.6: S-transform of hub displacement for operational loading: no scour case
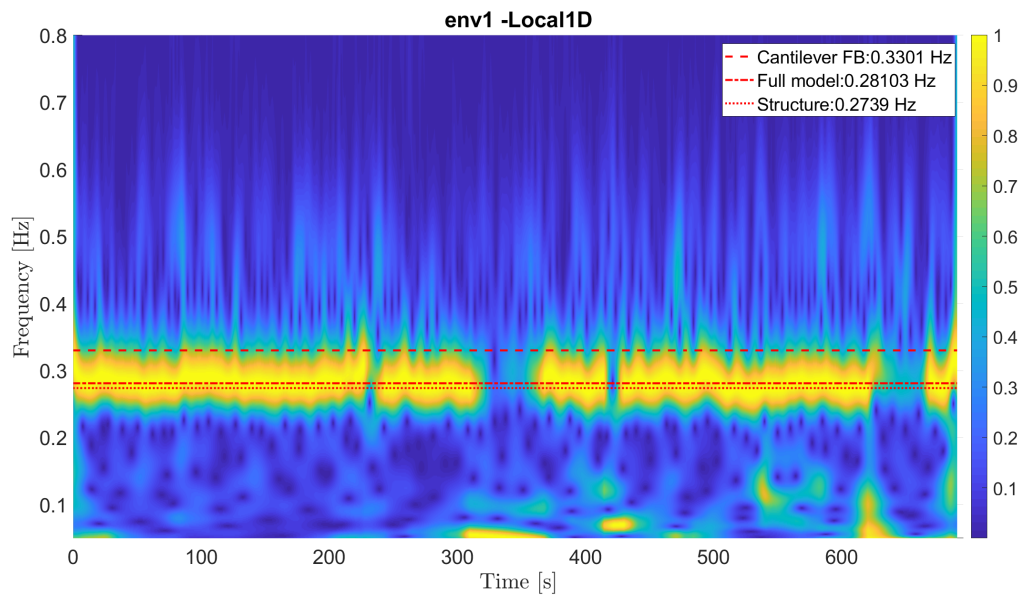
Figure 4.7: S-transform of hub displacement for operational loading: 1D local scour case
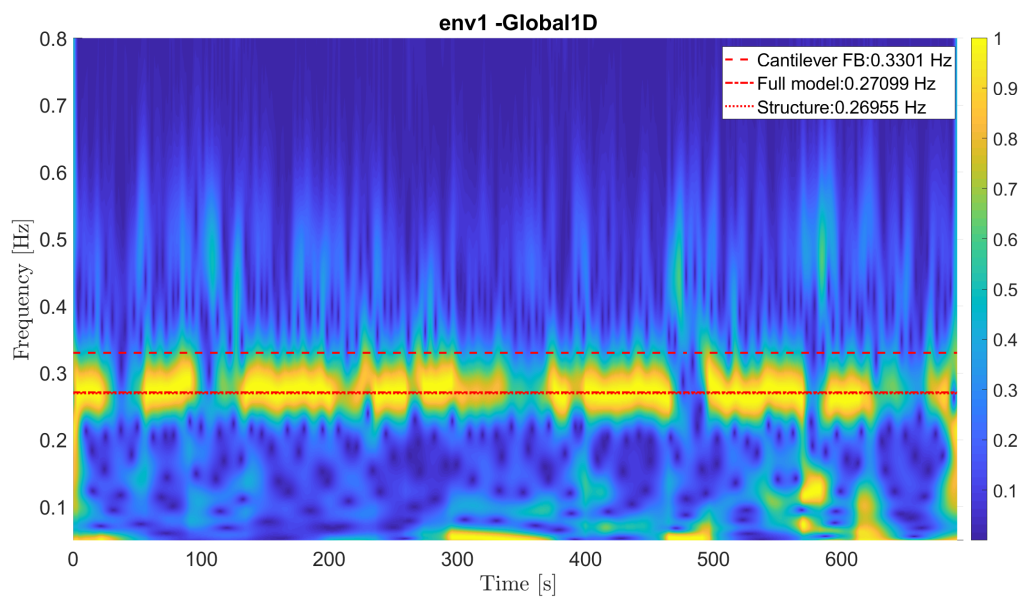

Figure 4.8: S-transform of hub displacement for operational loading: 1D global scour case

4.2.3. Damping

Two types of damping measurement are made: damping under free vibration due to impulse, and damping under a simulation of a 'rotor-stop' experiment. The rotor-stop is simulated for the cutoff environmental loading, by cutting of the load towards the end of the simulation and allowing the turbine to oscillate for 100 s (approximately 25 cycles). In both cases, the resulting oscillations are subjected to the log decrement method in order to extract a damping value.

The logarithmic decrement of a signal is defined as the natural logarithm of the ratio of the amplitudes of any two successive peaks of the signal.

$$\delta = \frac{1}{n} \frac{x(t)}{x(t+nT)} \tag{4.1}$$

Here, $x(t)$ is the amplitude at time t and $x(t + nT)$ is the amplitude of the peak n periods away - T being the period of the signal. From δ, the damping ratio of the system can then be found through equation 4.2.

$$\zeta = \frac{1}{1 + \sqrt{1 + \left(\frac{2\pi}{\delta}\right)^2}} \tag{4.2}$$

The trend lines of hub displacement under impulse for local and no scour cases is illustrated in figures 4.9 and 4.10 below. The corresponding damping values are found in table 4.3. The trends of damping across all models is discussed in detail in a later section.
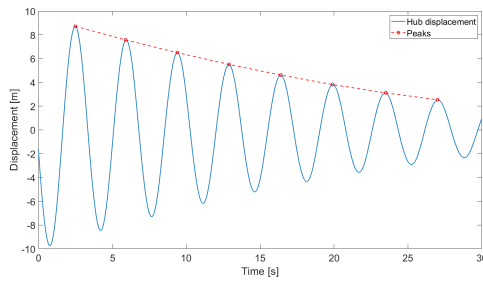

Figure 4.9: Hub displacement with marked peaks under impulse loading: no scour
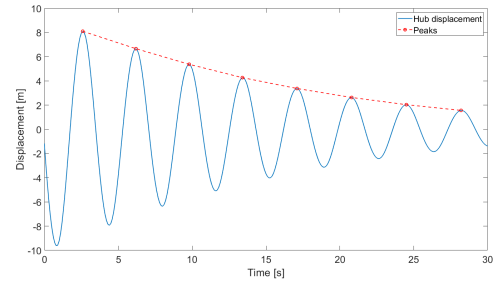
Figure 4.10: Hub displacement and with marked peaks under impulse loading: 1D local scour

4.2.4. Soil behaviour

The stress path and stress-strain curves of no scour and 1D scour cases is illustrated in figures 4.11 to 4.16. The cyclic behaviour is of soil is clearly observable in the figures.

Figure 4.11: Stress paths of $\tau_{xz} - p'$ for all control points: no scour, under operational loading. The colourbars indicate time in seconds.

Figure 4.12: Stress strain $\tau_{xz} - \gamma_{xz}$ for all control points: no scour, under operational loading. The colourbars indicate time in seconds.

Figure 4.13: Stress paths of $\tau_{xz} - p'$ for all control points: global 1D scour, under operational loading. The colourbars indicate time in seconds.

Figure 4.14: Stress strain $\tau_{xz} - \gamma_{xz}$ for all control points: global 1D scour, under operational loading. The colourbars indicate time in seconds.
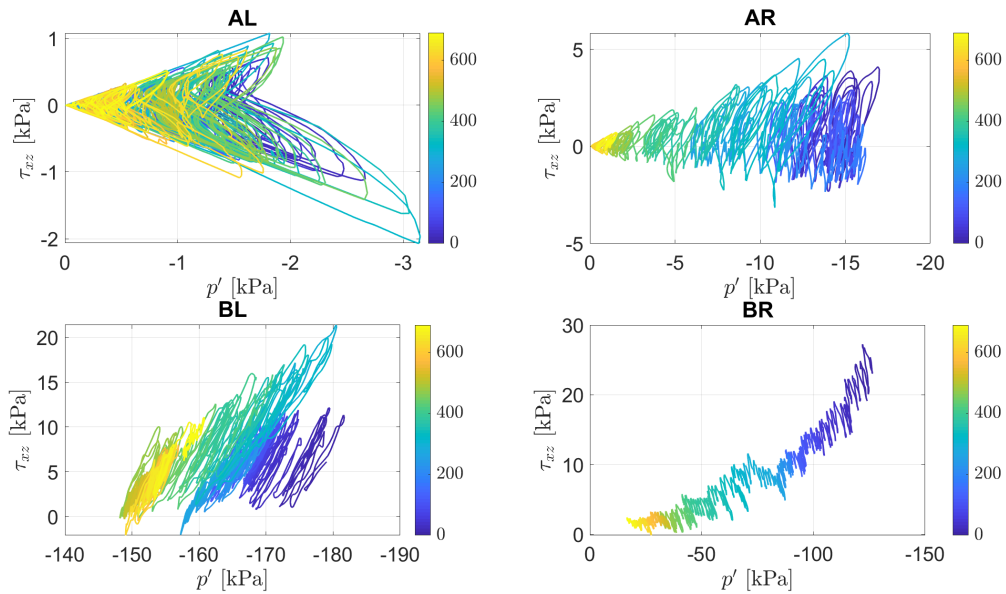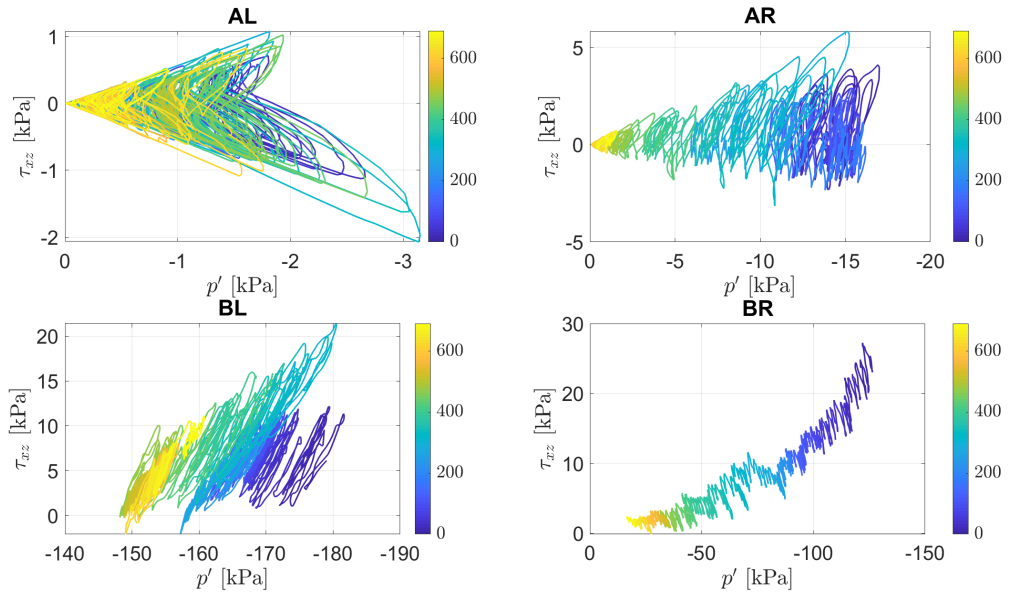
Figure 4.15: Stress paths of $\tau_{xz} - p'$ for all control points: local 1D scour, under operational loading. The colourbars indicate time in seconds.
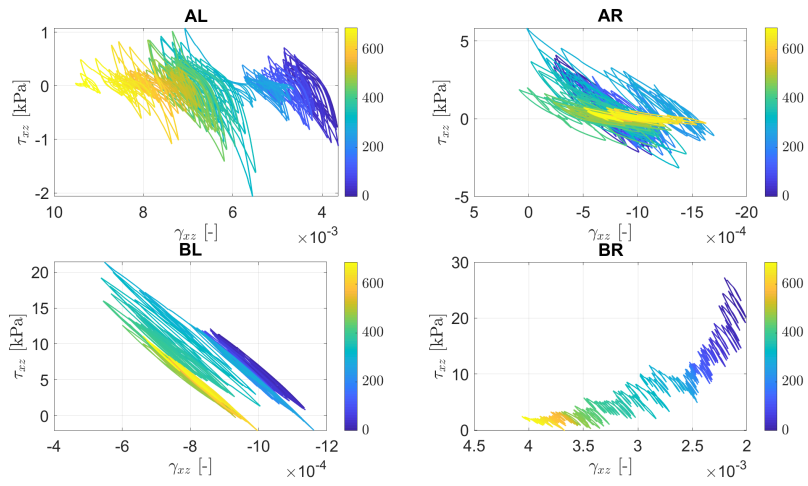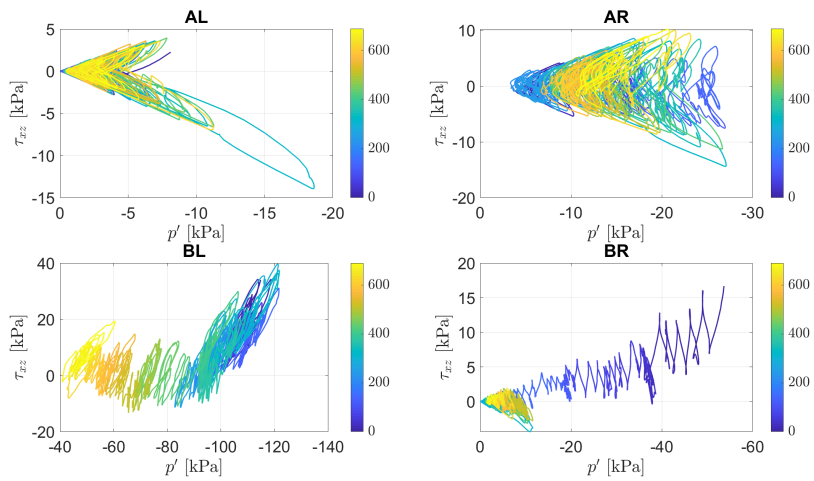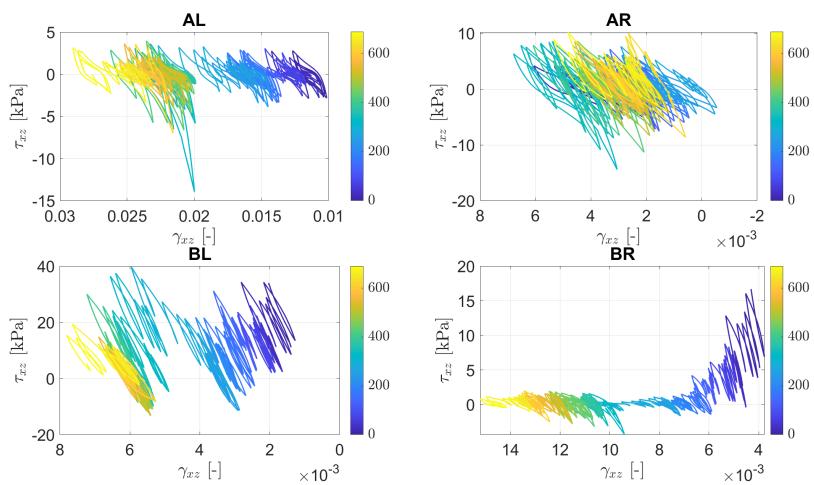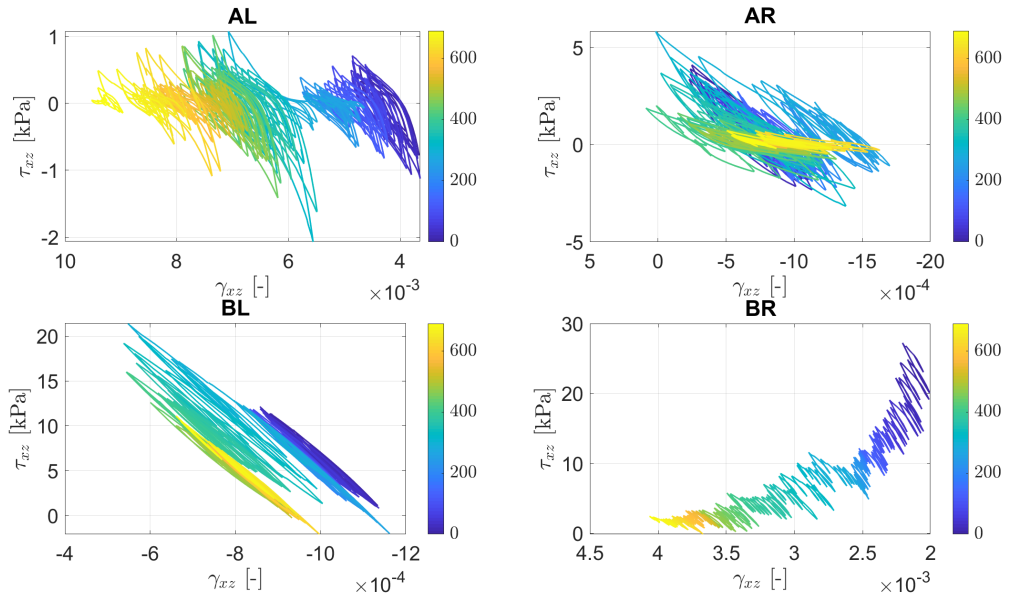

Figure 4.16: Stress strain $\tau_{xz} - \gamma_{xz}$ for all control points: local 1D scour, under operational loading. The colourbars indicate time in seconds.

For certain cases, observable changes are visible around the 400 second mark, which corresponds to a jump in the mean wind force - which is the dominant force in this system.

4.3. Evolution of pore water pressure for semi-drained condition

The no scour, 1.33D local scour and 1.33D global scour cases are examined for two permeabilites to evaluate the impact of pore water pressure. One of the permeabilities is low, in the order of 10^{-5}, similar to all other models in this study. As a comparison, a model with high permeability in the order of 10^{-3} is examined. It is expected that the latter case will show drained or semi-drained behaviour. All of these studies are under storm loading.
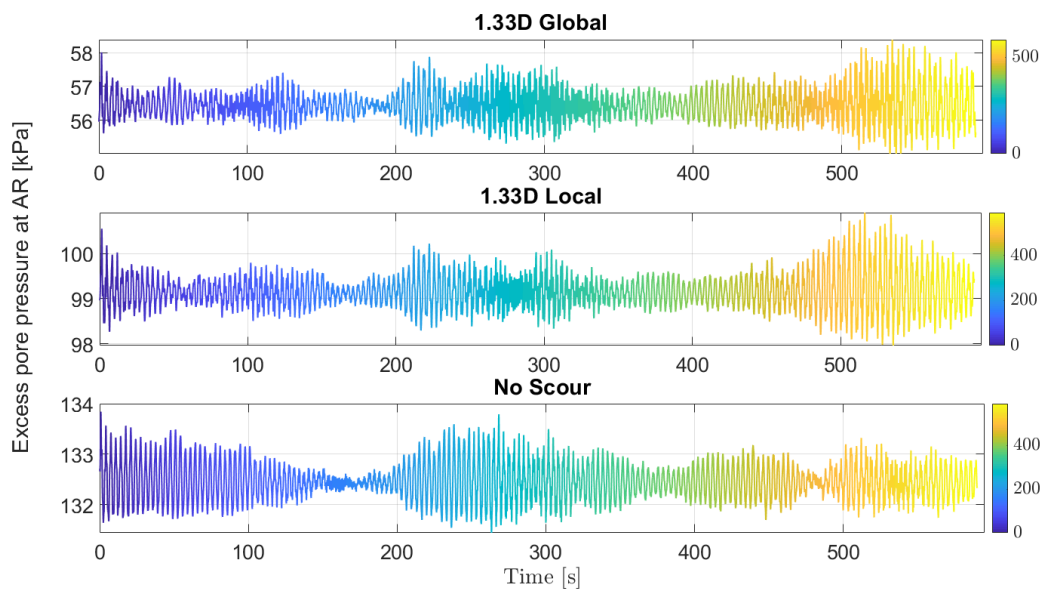
Figure 4.17: Evolution of pore water pressure for high permeability
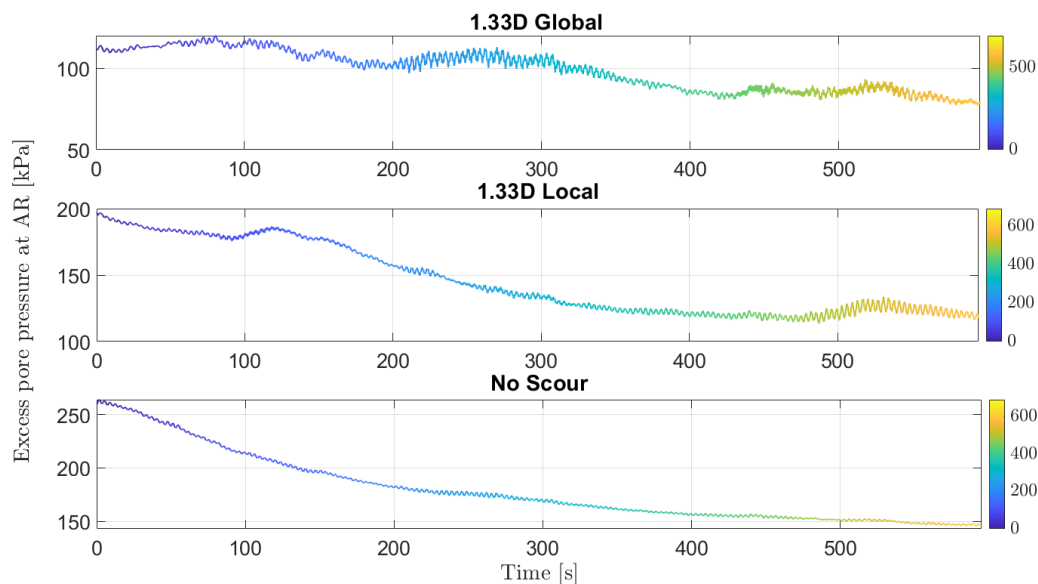
Figure 4.18: Evolution of pore water pressure for low permeability

The following observations are noted from the pore pressure behaviour:

- There is consistent decrease in pore pressure for the low permeability case - indicating the steady state has not been achieved yet (figure 4.17).

- Based on animated visualisations, the pore wwater pressure accumulates during ramping up of the load and at the end of ramp starts dropping considerably, in case of low permeability. For high permeability, there is probably no such excess pwp buildup during the ramp, and therefore the results are something similar to a steady state condition from the beginning (4.18).

- For high permeability case, a near constant u/p ratio is seen, in some cases after a period of slight increase. This is similar to the trend expected in steady state.

- It appears that under drained condition, local scour shows a pore water pressure behaviour closer to global scour than no scour (figure 4.19) near the surface. This could be a product of the fact that with

increase in scour depth, local scour behaviour moves closer to global scour - i.e. at a high depth like 1.33D, local scour behaviour is closer to global scour than no scour. This phenomenon is examined in the response frequency study in the next section.

- Based on the trends, to analyse soil behaviour for undrained condition more accurately, the ramp loading should be applied under a drained or semi-drained state, and then the permeability should be decreased.
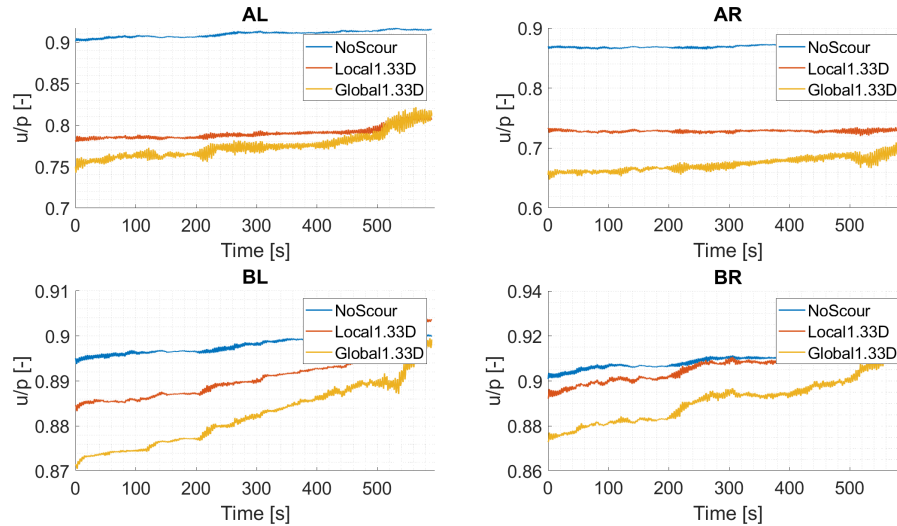
Figure 4.19: Evolution of pore water pressure as a fraction of total stress for high permeability
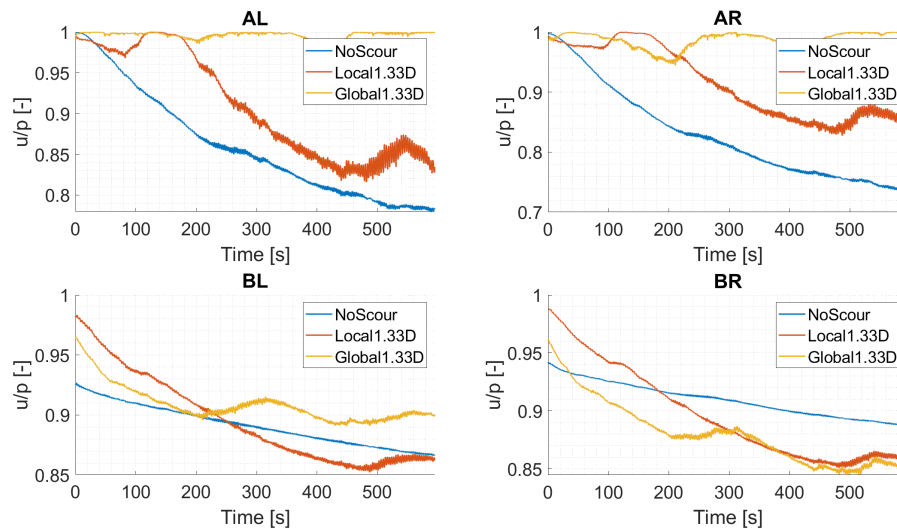
Figure 4.20: Evolution of pore water pressure as a fraction of total stress for low permeability

4.4. Trends: Response frequency

4.4.1. Linear elastic soil

In order to investigate the importance of non-linear soil model, an impulse loading of 1MN is applied to the model with both linear elastic soil and the non-linear model described in previous chapter. The results in figure 4.21 demonstrates that the captured variation between local and global scour is far more significant when the non-linear soil model is used.
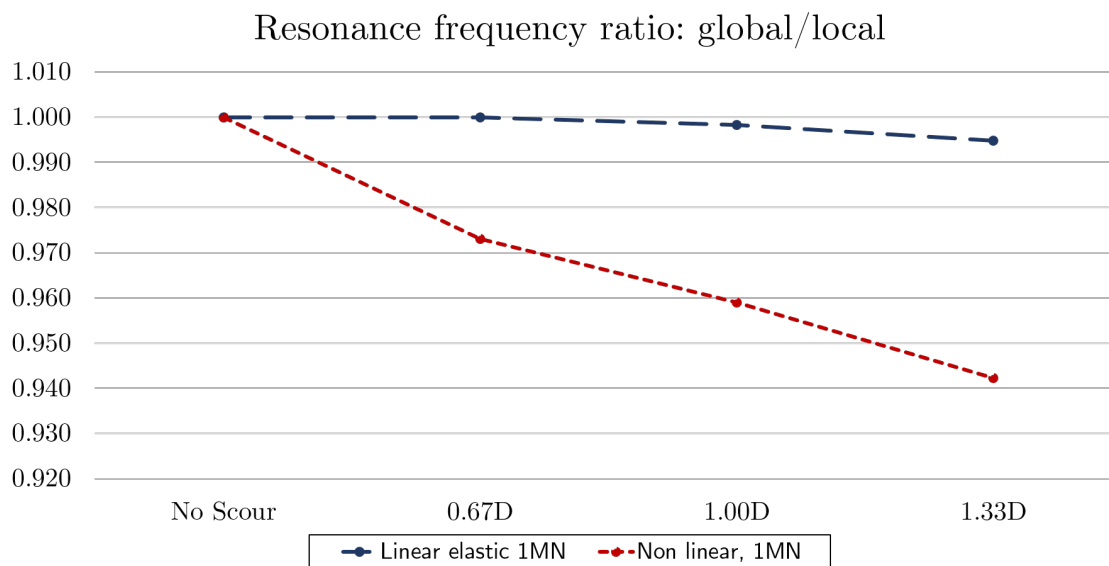
Figure 4.21: Resonance frequency under impulse of 1MN: all values normalized with respect to no scour condition

As real world soil shows non-linear elastoplastic behaviour under most circumstances, it is likely that the real world distinctions between global and local scour may be lost if the soil model is simplified to linear elastic during numerical analysis.

Also, in this model, the stiffness of the linear elastic soil is calibrated by varying the elastic modulus by trial and error, until the natural frequency for linear elastic soil matches that of the model with non-linear soil but under very small impulse loading (1 kN). This calibration is done for the no scour condition and the same elastic modulus is applied to the remaining models. If a model is required to use the linear elastic model, it might be necessary to recalibrate the soil for each scour condition individually, to get more realistic results.

4.4.2. Local vs global scour

It is observed that the resonance frequency is consistently higher for local scour than for global scour. While resonance frequency under global scour remains similar under all loading conditions, the local scour increases considerably - from around $1.5 - 2\%$ for lower scour depths under operational loading, to over 8% for higher scour depths with loads in the cut-off region. The trends are also illustrated in figures 4.23 and 4.22.

Table 4.6: Percentage increase in (resonant) response frequency of local scour, with respect to global scour

% decrease in global scour (resonant) response frequency with respect to local scour			
Scour Depth	Impulse load 9MN	Operational load	Cut-off load
0.67D	1.57	1.44	1.98
1D	1.59	3.69	8.41
1.33D	3.39	3.10	8.33

The consistent increase in the gaps is due to the corresponding consistent increase in resonance frequency under local scour. Local scour seems closer to global scour under the higher operational loads, but seems to move away for loads in the cut-off region.
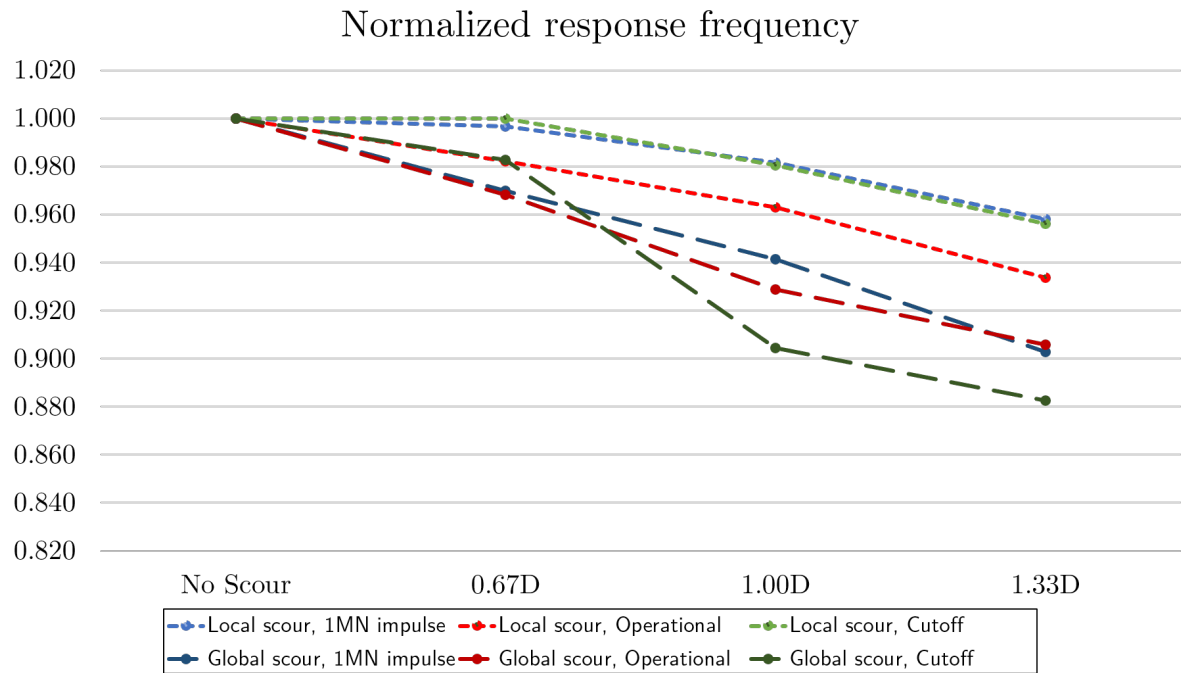
Figure 4.22: Resonance frequency trend under environmental loading: normalized with respect to no scour conditions

4.4.3. Scour depth

The table 4.7 shows that resonance frequency steadily decreases with increase in scour depth. The effect is more pronounced for global scour than local scour. Other influences of scour depth (on local vs global scour, on damping, etc) are discussed in other sections of this chapter.

Table 4.7: Percentage decrease in resonance frequency with respect to no scour condition

Scour Depth	Impulse 9MN		Opertional		Cut-off	
	Global	Local	Global	Local	Global	Local
0.67D	4.53	3.03	3.18	1.78	1.72	-0.22
1D	6.03	4.53	7.13	3.70	9.54	1.93
1.33D	10.60	7.56	9.42	6.61	11.74	4.38

4.4.4. Influence of loading ramp

Assuming that the higher permeability case is steady state while the lower permeability is not, it is interesting to examine the influence on resonance frequency for the two cases. From table 4.8, it is noted that the no scour and local scour cases show negligible difference. However, the global scour under lower permeability is more than 7% lower than that for higher permeability. The overall trend of local scour frequencies lying between no scour and global scour is still preserved however, with the global scour frequency being the lowest of the three.

Table 4.8: Change in resonance frequency for different permeabilities, under storm loading

Model	Permeability = 1.00E-05 m^3/day	Permeability = 1.00E-03 m^3/day	% change
No Scour	0.2975 Hz	0.29922 Hz	0.57
1.33D Local	0.2858 Hz	0.28725 Hz	0.50
1.33D Global	0.2646 Hz	0.28493 Hz	7.13

4.4.5. Magnitude of force

The magnitude of applied force also seems to have an impact on the resonance frequency. Results for three impulse loads: 1 kN, 1MN and 9MN are compared in figure 4.23 for reference.
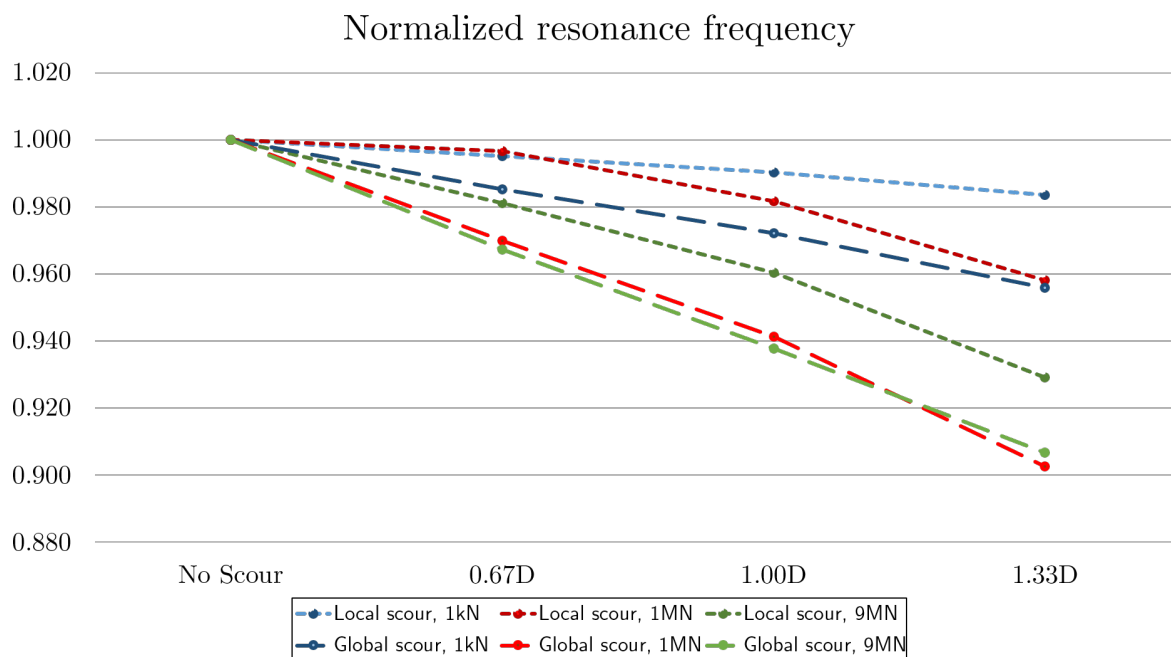

Figure 4.23: Resonance frequency trend under different magnitudes of impulse loading: normalized with respect to no scour conditions

The increase in forcing magnitude appears to cause the resonance frequency to diverge further from no scour scour condition, overall. The drop in frequency with scour depth occurs at an accelerated pace.

4.5. Trends: Damping ratio

Damping ratio for the fixed base cantilever is negligible, in the order of 0.05%. Thus the trends are evaluated relative to the no scour condition. The trends are illustrated in figure 4.24. The damping coefficient, normalized with respect to the no scour condition, is also evaluated and listed in table **??**

Table 4.9: Damping ratio under different impulse loads, normalized with respect to damping ratio under no scour conditions

Scour Depth	Linear Elastic, 1MN		Non linear, 1 kN		Non linear, 1MN		Non linear, 9MN	
	Local	Global	Local	Global	Local	Global	Local	Global
No Scour	1.00	1.00	1.00	1.00	1.00	1.00	1.00	1.00
0.67D	0.14	0.13	0.00	0.00	1.12	1.71	1.11	1.36
1.00D	0.12	0.11	0.00	0.00	1.46	2.45	1.33	1.69
1.33D	0.14	0.15	0.00	0.00	2.04	3.40	1.95	2.20

The damping ratio under impulse generally increases with increase in scour depth for non linear soil. Although the volume of soil in the domain is reduced more for global scour rather than local scour, the dominating influence is the increased plasticity in soil due to higher lateral movement by the OWT. As demonstrated in literature ([16]), for small cyclic strains the equivalent damping ratio of soil increases with increase in plasticity. The large amplitude of non-linear displacements in the current soil model causes a corresponding decrease in stiffness. With vibrations of larger amplitude, there is larger hysteresis loss in energy and thus there is greater damping with increased displacements.
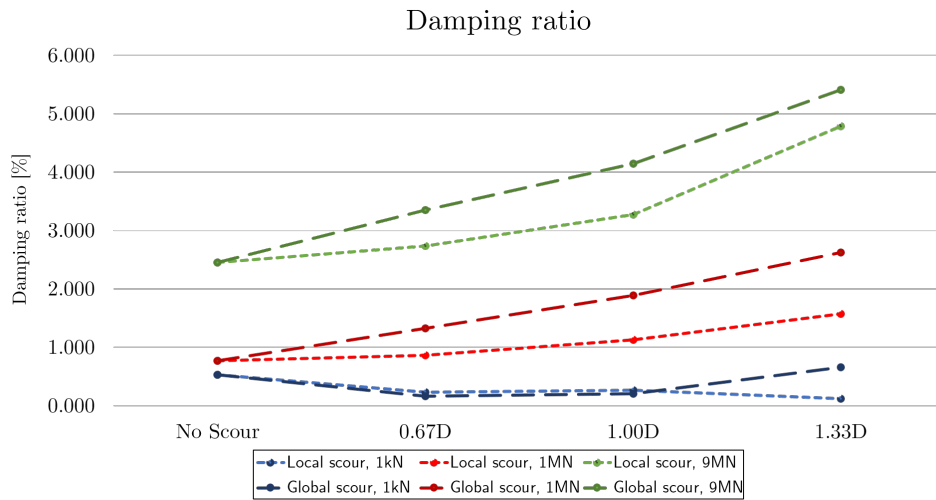
Figure 4.24: Damping trends under impulse loading: all magnitude in %

For similar reasons (i.e., larger displacement amplitude), an increase in magnitude of load also shows higher damping. The damping under global scour is also consistently higher than local scour - except with 1kN, where the load is too small to cause appreciable damping initially. However at high scour depths where damping does start to be substantial, global scour shows higher damping than local.

However, in considering the 1kN loading case, it is noted that the damping ratio slightly drops initially, before returning to the trend shown by the other load cases at scour depths over 1D. This suggests that while in medium-high load cases the hysteretic loss is the dominant mechanism, a competing mechanism might exist at very low loading scenarios. At 1kN, the soil possibly does not develop sufficient non-linearity to the trends expected due to hyteresis loss, and hence the primary mechanism is probably the removal of soil, wherein lower soil volume results in lower damping. This changes at higher scour depths where non-linearity is developed and hysteresis comes into play once again.

A final note in case of damping should be made: damping in this study was discussed on the basis of damping ratio rather than the damping coefficient. However, upon analysing the damping coefficient (normalized with respect to no scour condition) instead of ratio for all the models, the trends are seen to be nearly identical (figure 4.25). Thus the natural frequency component of the damping ratio does not have any substantial influence. The corresponding figures for damping coeffcient - normalized with respect to the no scour condition - is in table 4.10.
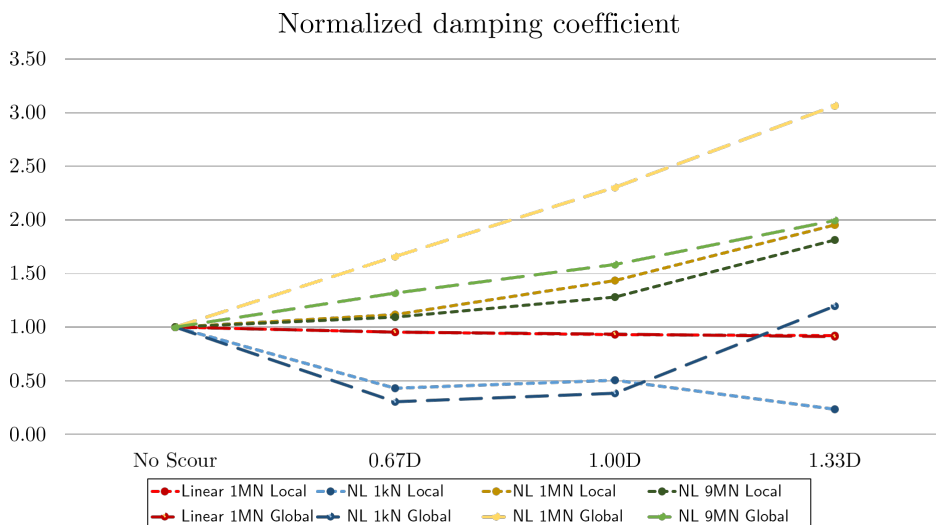

Figure 4.25: Damping trends under impulse loading: all magnitude in %

Table 4.10: Damping coefficient normalised with respect to no scour condition

Model	Linear Elastic, 1MN		Non linear, 1 kN		Non linear, 1MN		Non linear, 9MN	
	Local	Global	Local	Global	Local	Global	Local	Global
No Scour	1.00	1.00	1.00	1.00	1.00	1.00	1.00	1.00
0.67D	0.95	0.95	0.43	0.30	1.12	1.66	1.09	1.32
1.00D	0.93	0.94	0.51	0.38	1.43	2.30	1.28	1.58
1.33D	0.92	0.91	0.23	1.20	1.95	3.07	1.81	2.00

5

Conclusions

To return to the research question formulated in chapter 2, the following conclusions can be formulated.

A. Does scour have a substantial impact on the resonance frequency of a turbine?

- Scour can indeed have a substantial impact on resonance frequency: within the depth of range 1D-1.33D, resonance frequency is seen to drop by over 10% relative to no scour condition in this study. However, the frquencies despite the drop remain at a magnitude of 0.25 Hz or higher: thus, there is no concern over resonance with wave frequencies or 1P frequency (both in the range of 0.1 - 0.2 Hz).

- In addition, it should be noted that high drops beyond $3-4\%$ occur only for very high scour depths - in this case in the range $9-12m$, and the existence of such high depths offshore in reality is transient at best, considering real world scour is not a static depth and there is constant backfilling occurring in the ocean.

B. How does the impact differ for local scour and global scour under different depths?

- The frequency generally decreases with increase in scour depth. Global scour shows a higher decrease than local scour. However, this gap between local and global scour generally decreases with increase in scour depth.

- Upon examination of the time evolution of resonant frequency, global scour is also seemingly disrupted by the environmental conditions more easily than local scour. The resonance frequency under global scour drops to the $0.04-0.1Hz$ level (corresponding to environmental loading) far more often than local scour, if the time evolution of the frequency is examined.

C. Is non-linear soil important for these examinations?

- The differences between local and global scour conditions is much more prominent under a non-linear soil model, relative to a linear elastic soil model. Thus for study of differences between local and global scour, use of a non-linear soil model is recommended.

D. Does scour have an impact on the damping of the OWT in non linear soil?

- The damping ratio generally increases with an increase in scour depth, due to higher displacements causing an increased hysteresis loss in the non-linear soil. In contrast, the linear elastic soil shows virtually no difference in damping for the two cases.

- With very low loads - and therefore low non-linearity - there is a small drop in damping, which suggests that a competing mechanism might exists besides the increase in displacement causing increased plasticity. This phenomenon would require further investigation before conclusive evidence can be obtained.

5.1. Further research

In a follow up to the research presented here, some additional directions may be considered for the future:

- Modelling of scour: as opposed to a fixed maximum depth, the examination of time evolution of frequencies allows alteration of scour depth at different points in time. This might be a useful way to look at effects like backfilling while also considering the timescale of its occurrence.

- Similarly, a modelling of hydrodynamic loads under scour with the use of a full 3D FEM simulation could also be a possible direction of research.

- The evaluation of dynamic response can be extended to examine the fatigue design of monopiles under scour.

- Impact of wider scour (where bottom diameter of the hole is larger than pile diameter), as well as non-conical scour hole shapes can be assessed.

Bibliography

[1] Christian Bak, Frederik Zahle, Robert Bitsche, Taeseong Kim, Anders Yde, Lars Christian Henriksen, Morten Hartvig Hansen, Jose Pedro Albergaria Amaral Blasques, Mac Gaunaa, and Anand Natarajan. The dtu 10-mw reference wind turbine. In *Danish Wind Power Research 2013*, 2013.

[2] Erik Damgaard Christensen and Henrik Bredmose. Scour holes or scour protection around offshore wind turbine foundations: Effect on loads. In *2007 European Wind Energy Conference and Exhibition*, 2007.

[3] International Electrotechnical Commission et al. Wind turbines: Part 1: Design requirements; 2005, 2005.

[4] Yannis F Dafalias and Majid T Manzari. Simple plasticity sand model accounting for fabric change effects. *Journal of Engineering mechanics*, 130(6):622–634, 2004.

[5] Det Verorske Veritas DNV. Dnv-os-j101 offshore standard: Design of offshore wind turbine structures. *DNV AS, H o vik, Norway*, 2011.

[6] David Foxwell. Ge employees ready to start building next-generation super blade, 2018. URL https://www.owjonline.com/news/view, ge-employees-ready-to-start-building-nextgeneration-super-blade_56020.htm.

[7] David Foxwell. Technology can take us to 20 mw, turbine and blade builders say, 2018. URL https://www.owjonline.com/news/view, technology-can-take-us-to-20-mw-turbine-and-blade-builders-say_55758.htm.

[8] Alborz Ghofrani and Pedro Arduino. Prediction of leap centrifuge test results using a pressure-dependent bounding surface constitutive model. *Soil Dynamics and Earthquake Engineering*, 113:758–770, 2018.

[9] Les Hamill. *Bridge hydraulics*. CRC Press, 2014.

[10] John Marius Hegseth and Erin E Bachynski. A semi-analytical frequency domain model for efficient design evaluation of spar floating wind turbines. *Marine Structures*, 64:186–210, 2019.

[11] Maosong Huang, Zhong Qi Yue, LG Tham, and OC Zienkiewicz. On the stable finite element procedures for dynamic problems of saturated porous media. *International Journal for Numerical Methods in Engineering*, 61(9):1421–1450, 2004.

[12] Jason Jonkman, Sandy Butterfield, Walter Musial, and George Scott. Definition of a 5-mw reference wind turbine for offshore system development. Technical report, National Renewable Energy Lab.(NREL), Golden, CO (United States), 2009.

[13] Madjid Karimirad. Marintek numerical tools for coupled aero-hydro-servo-elastic simulations of offshore wind turbines. 2012.

[14] A. T. Kearney. Wind power, 2018. URL http://www.energy-transition-institute.com/Insights/Wind.html.

[15] Evangelos Kementzetzidis, Willem Geert Versteijlen, Axel Nernheim, and Federico Pisanò. 3d fe dynamic modelling of offshore wind turbines in sand: natural frequency evolution in the pre–to after-storm transition. In *Numerical Methods in Geotechnical Engineering IX, Volume 2*, pages 1477–1484. CRC Press, 2018.

[16] Giuseppe Lanzo and MLADEN VUCETIC. Effect of soil plasticity on damping ratio at small cyclic strains. *Soils and Foundations*, 39(4):131–141, 1999.

[17] Q Li, LJ Prendergast, A Askarinejad, and K Gavin. Effect of scour on the behavior of a combined loaded monopile in sand. In *9th European Conference on Numerical Methods in Geotechnical Engineering*, 2018.

[18] HY Liu, JA Abell, A Diambra, and F Pisano. A three-surface plasticity model capturing cyclic sand ratcheting. *Géotechnique submitted for publication*, 2018.

[19] HY Liu, F Zygounas, A Diambra, and F Pisano. Enhanced plasticity modelling of high-cyclic ratcheting and pore pressure accumulation in sands. In *Numerical Methods in Geotechnical Engineering IX, Volume 1: Proceedings of the 9th European Conference on Numerical Methods in Geotechnical Engineering (NUMGE 2018), June 25-27, 2018, Porto, Portugal*, page 87. CRC Press, 2018.

[20] RC MacCamy and R Aam Fuchs. Wave forces on piles: a diffraction theory. Technical report, Corps of Engineers Washington DC Beach Erosion Board, 1954.

[21] Majid T Manzari and Yannis F Dafalias. A critical state two-surface plasticity model for sands. *Geotechnique*, 47(2):255–272, 1997.

[22] Clara Matutano, Vicente Negro, Jose-Santos López-Gutiérrez, and M Dolores Esteban. Scour prediction and scour protections in offshore wind farms. *Renewable energy*, 57:358–365, 2013.

[23] Christopher R McGann, Pedro Arduino, and Peter Mackenzie-Helnwein. A stabilized single-point finite element formulation for three-dimensional dynamic analysis of saturated soils. *Computers and Geotechnics*, 66:126–141, 2015.

[24] JR Morison, JW Johnson, SA Schaaf, et al. The force exerted by surface waves on piles. *Journal of Petroleum Technology*, 2(05):149–154, 1950.

[25] Nathan Mortimore Newmark et al. A method of computation for structural dynamics. American Society of Civil Engineers, 1959.

[26] OpenSees. Manzari dafalias material - openseeswiki 2019, 2019. URL `http://opensees.berkeley.edu/wiki/index.php/Manzari_Dafalias_Material`.

[27] LJ Prendergast, C Reale, and K Gavin. Probabilistic examination of the change in eigenfrequencies of an offshore wind turbine under progressive scour incorporating soil spatial variability. *Marine Structures*, 57:87–104, 2018.

[28] Luke J Prendergast, David Hester, Kenneth Gavin, and JJ O'sullivan. An investigation of the changes in the natural frequency of a pile affected by scour. *Journal of Sound and Vibration*, 332(25):6685–6702, 2013.

[29] Luke J Prendergast, Kenneth Gavin, and Paul Doherty. An investigation into the effect of scour on the natural frequency of an offshore wind turbine. *Ocean Engineering*, 101:1–11, 2015.

[30] WG Qi, FP Gao, MF Randolph, and BM Lehane. Scour effects on p–y curves for shallowly embedded piles in sand. *Géotechnique*, 66(8):648–660, 2016.

[31] Michael H Scott and Gregory L Fenves. A krylov subspace accelerated newton algorithm. In *Proc., 2003 ASCE Structures Congress*, 2003.

[32] Scott W Sloan. Substepping schemes for the numerical integration of elastoplastic stress–strain relations. *International journal for numerical methods in engineering*, 24(5):893–911, 1987.

[33] Søren Peder Hyldal Sørensen and Lars Bo Ibsen. Assessment of foundation design for offshore monopiles unprotected against scour. *Ocean Engineering*, 63:17–25, 2013.

[34] Tim Raaijmakers. *Scour and scour protection for offshore wind support structures*. Lecture Slides for OE44135, Delft University of Technology, 2017. OE44135 Offshore Wind Support Structures.

[35] Joey Velarde and Erin E Bachynski. Design and fatigue analysis of monopile foundations to support the dtu 10 mw offshore wind turbine. *Energy Procedia*, 137:3–13, 2017.

[36] Zhi-Liang Wang, Yannis F Dafalias, and Chih-Kang Shen. Bounding surface hypoplasticity model for sand. *Journal of engineering mechanics*, 116(5):983–1001, 1990.

[37] WindEurope. Offshore wind in europe–key trends and statistics 2017, 2018.

[38] O Zienkiewicz, R Taylor, and JZ Zhu. Generalization of finite element concepts. galerkin weighted residual and variational approaches. *Finite element method*, 1:39–citation_lastpage, 2000.

[39] OC Zienkiewicz, CT Chang, and P Bettess. Drained, undrained, consolidating and dynamic behaviour assumptions in soils. *Geotechnique*, 30(4):385–395, 1980.

[40] Olgierd C Zienkiewicz, AHC Chan, M Pastor, BA Schrefler, and T Shiomi. *Computational geomechanics*. Citeseer, 1999.
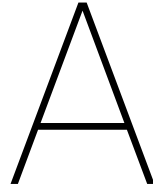
Mesh selection

A.1. No scour condition

Considering that the available computational capacity does not allow for a very fine mesh which approximates the size of actual soil particles, four different meshes (A-D) for the no scour were tested to arrive at a meshing solution which is computationally feasible. The relevant characteristics are tabulated in table , and they can be visualized in figures A.2 to A.6. As a point of reference, an overtly coarse mesh X is also tested, as shown in figure A.1.
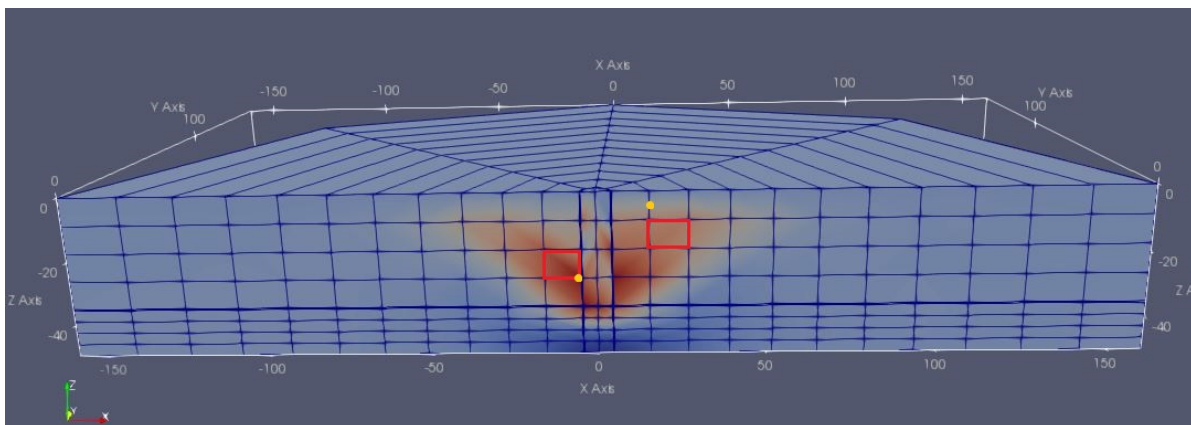
Figure A.1: Mesh X0. Control elements (A = right, B = left) marked in red, control nodes (A = right, B = left) marked in yellow.
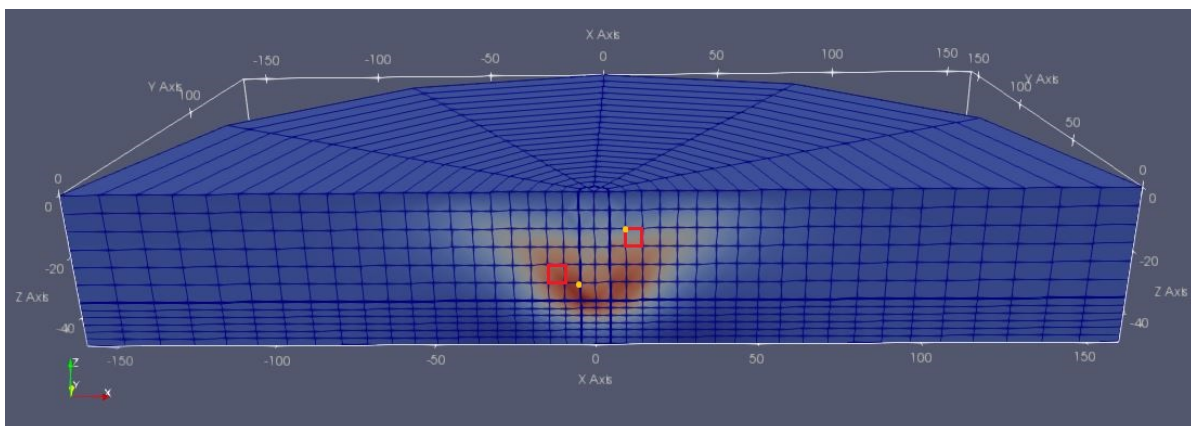
Figure A.2: Mesh A0. Control elements marked in red (A = right, B = left), control nodes (A = right, B = left) marked in yellow.
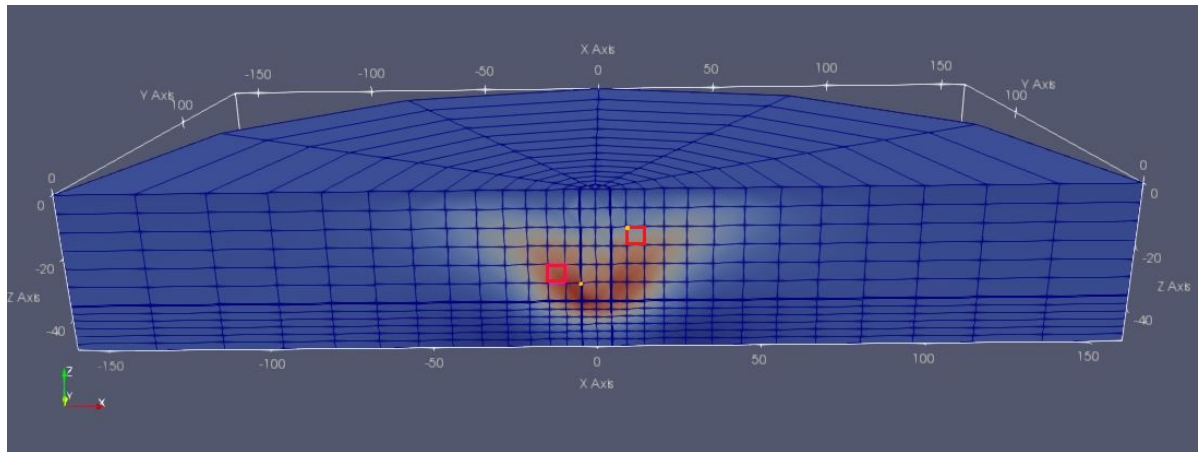
Figure A.3: Mesh B0. Control elements (A = right, B = left) marked in red, control nodes (A = right, B = left) marked in yellow.
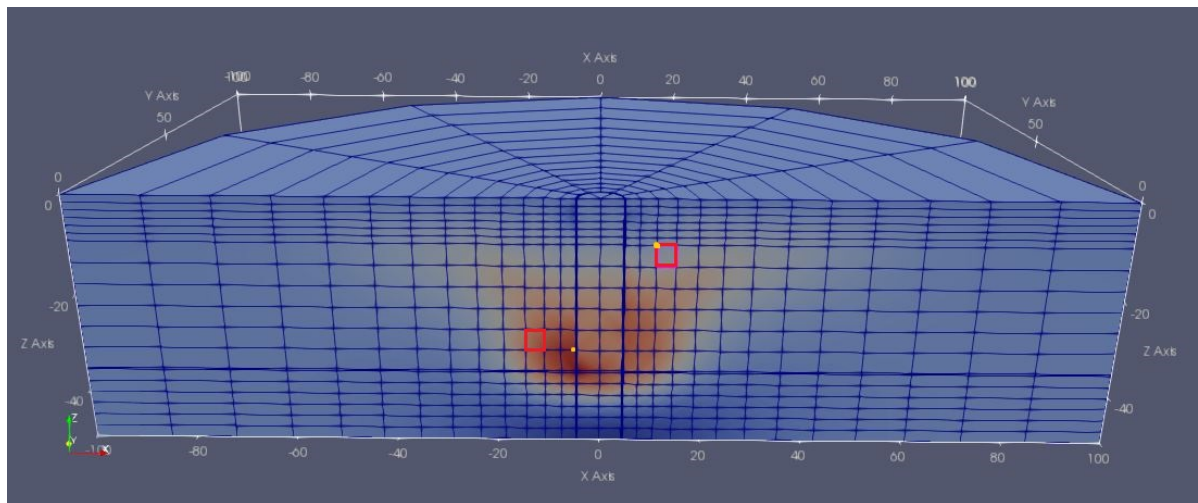
Figure A.4: Mesh C0. Control elements (A = right, B = left) marked in red, control nodes (A = right, B = left) marked in yellow.
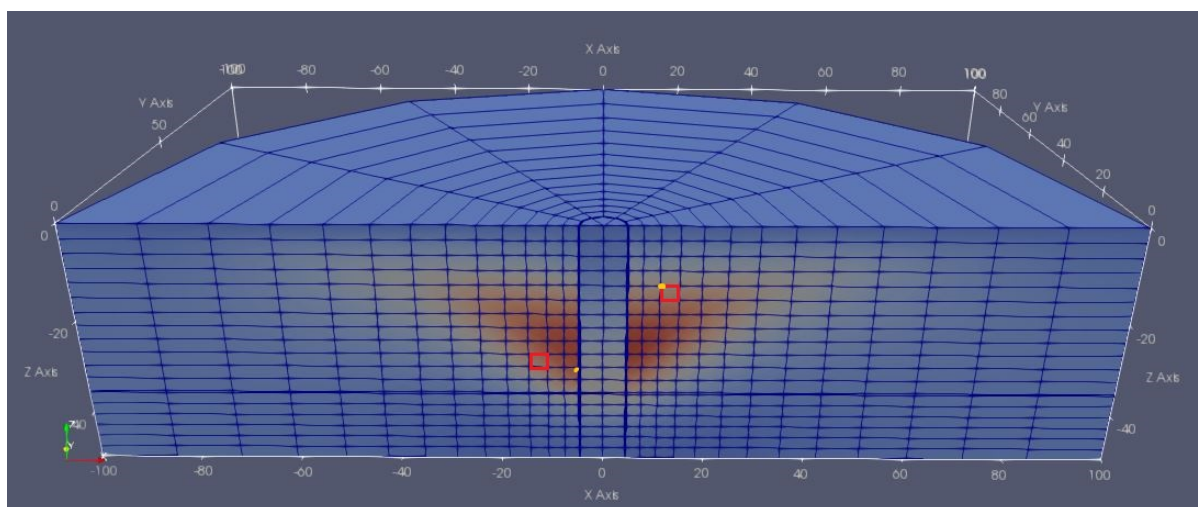

Figure A.5: Mesh C2. Control elements (A = right, B = left) marked in red, control nodes (A = right, B = left) marked in yellow.
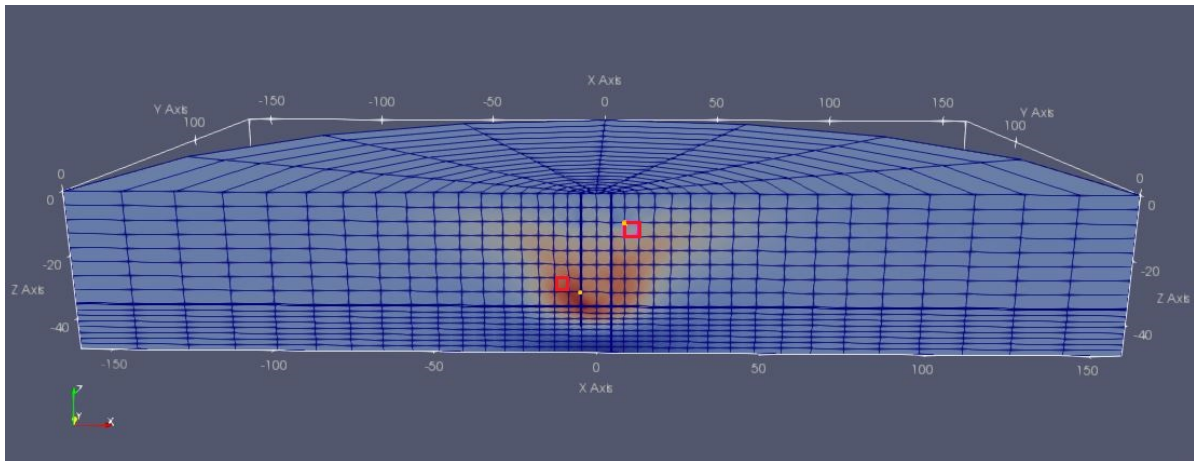
Figure A.6: Mesh D0. Control elements (A = right, B = left) marked in red, control nodes (A = right, B = left) marked in yellow.

The generated meshes are subjected to the following loading conditions (illustrated in figures A.7 to A.10):

1. Impulse loading of 9 MN applied at hub, 25 s

2. Sinusoidal loading about 0 MN mean applied at hub, 70 s

3. Sinusoidal loading about 1 MN mean applied at hub, 100 s

4. Turbulent wind loading at V_{wind} = 12 m/s applied at hub, 150 s

It should be noted that the meshes C0 and C2 (figure A.5) were tested for the same loads - C2 is a version of Mesh C0 but with a more even vertical distribution of elements. However, both meshes are found to have the same response in some cases - thus in figures where '7node0Dc2' is not present in the legend, the '7node0Dc' values represent both these meshes.
The results are compared on the basis of the following parameters:

a. Global displacement: at hub node and mudline node

b. Local displacement: at local nodes A and B

c. Pore water pressure development at local nodes A and B

d. Stress strain behaviour at control elements A and B

Mesh	X	A	B	C	D
Label in figures	5node0D	7node0Da	7node0Db	7node0Dc	9node0D
Domain height [m]	56	56	56	56	56
Domain radius [m]	160	160	160	100	160
Nodes	710	2268	1582	2260	3258
Elements	468	1755	1209	1767	2652
Refinement	N/A	N/A	Closer to pile	Closer to pile	N/A
Computation time	106 min	889 min	474 min	649 min	1327 min

Table A.1: Properties of different meshes. Note: Computation time in the table is for load case 2
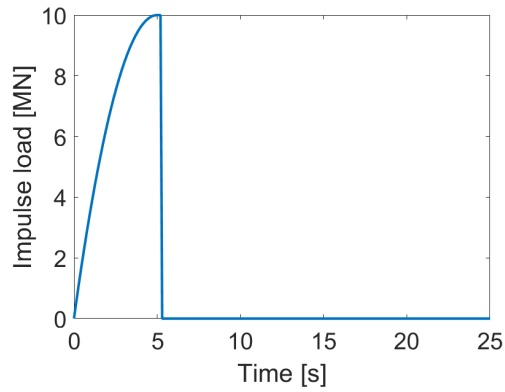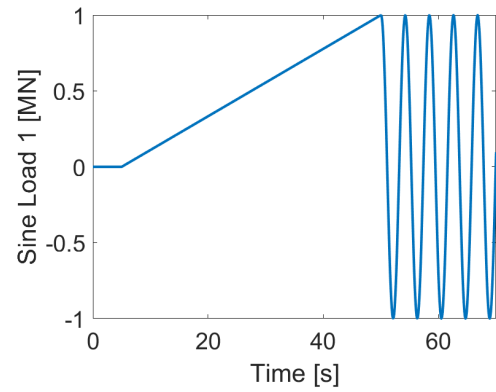
Figure A.7: a) Impulse loading
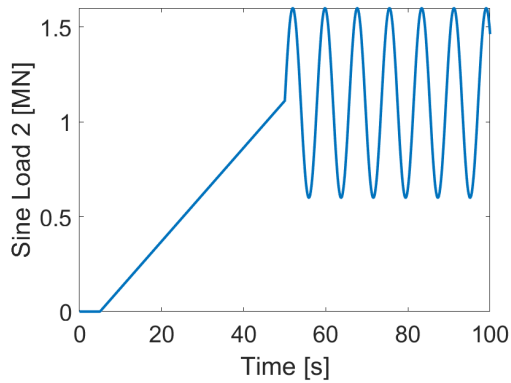

Figure A.8: b) Sinusoidal loading 1

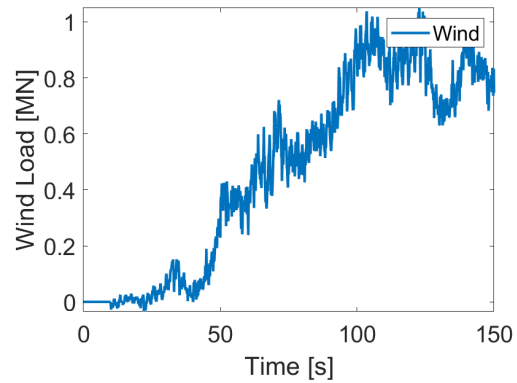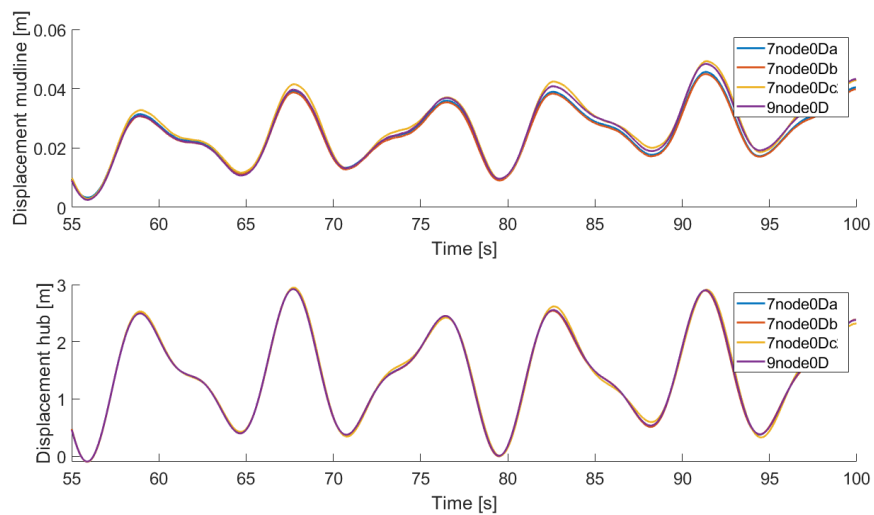Figure A.9: c) Sinusoidal loading 2

Figure A.10: d) Wind loading, V_{wind} = 12 m/s

Figure A.11: Global displacements for load case 3

The global displacement for all loads is found to be very similar. As a sample, the displacements for load case 3 is shown in figure A.11. Also in the interest of brevity, only selected results for the remaining parameters are illustrated in the other figures. The remaining results do not make any additional contribution to the mesh selection analysis.
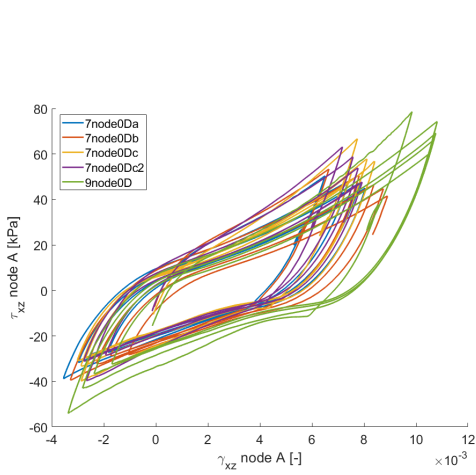
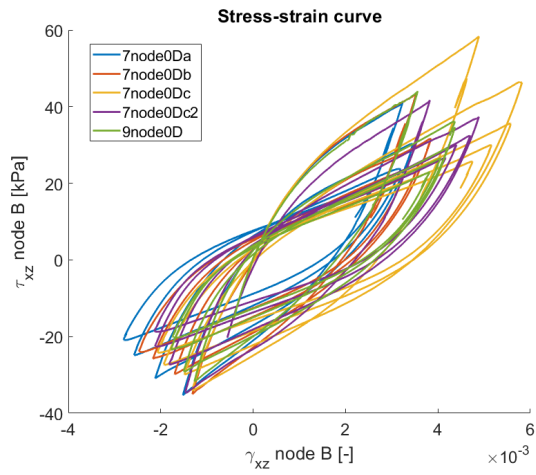Figure A.12: Stress-strain behaviour at element A under impulse load

Figure A.13: Stress-strain behaviour at element B under impulse load
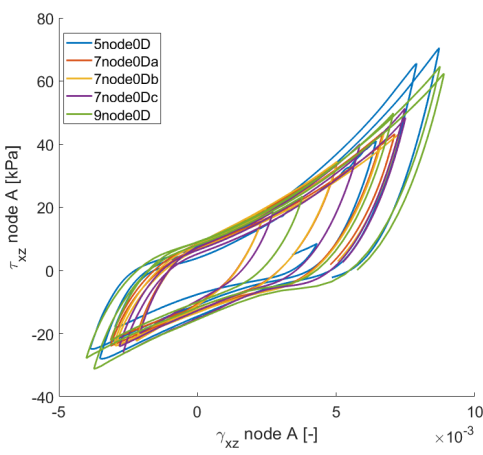

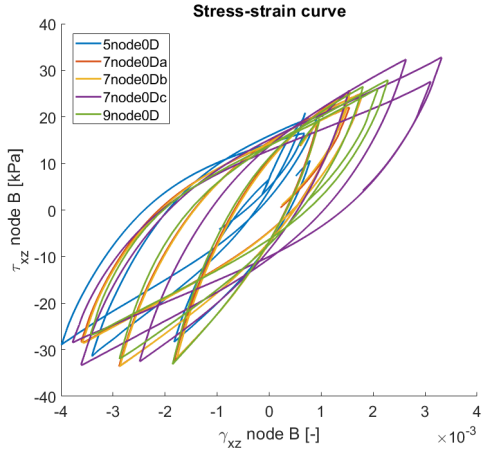Figure A.14: Stress-strain behaviour at element A under sine load 1

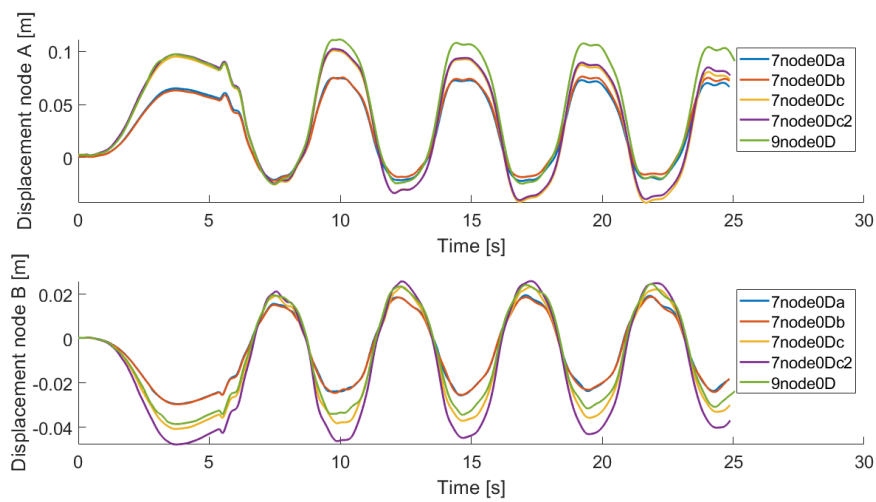Figure A.15: Stress-strain behaviour at element B under sine load 1

Figure A.16: Local displacement under impulse load

When looking at soil behaviour, it is specifically interesting to look at the results from load cases 1 and 2 due to the cyclic nature of the loading. As seen in figures A.12, A.13, A.14 and A.15, the cyclic behaviour of soil is approximately within a similar range for all meshes, in case of both elements. Due to different sizing and distribution of elements, the control elements do not correspond to the exact same position for all the meshes, and this contributes to the visible deviations.
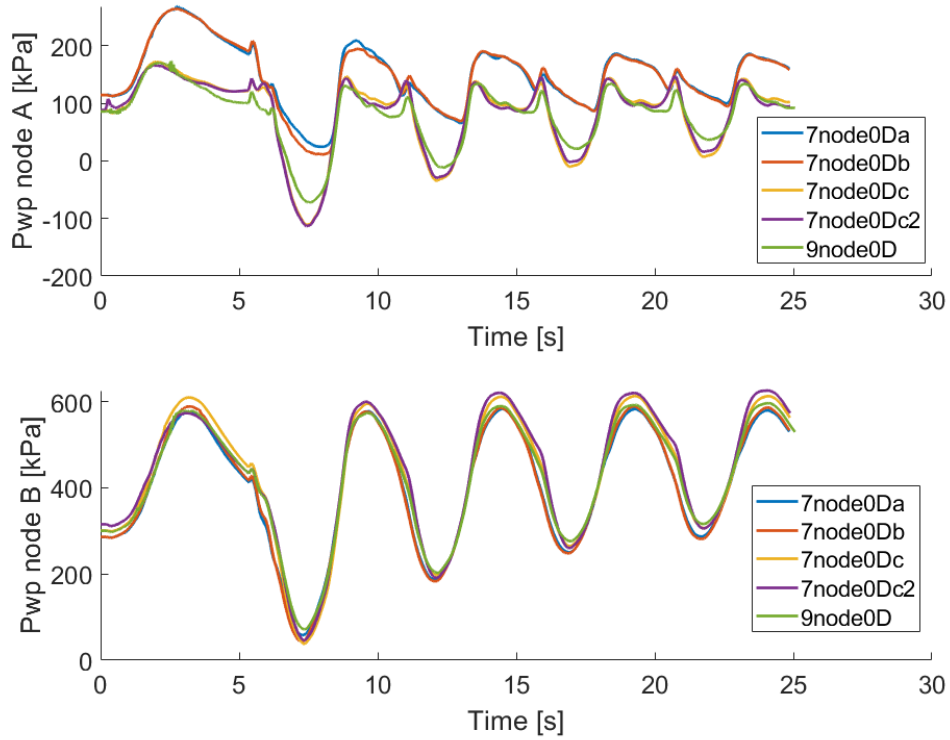
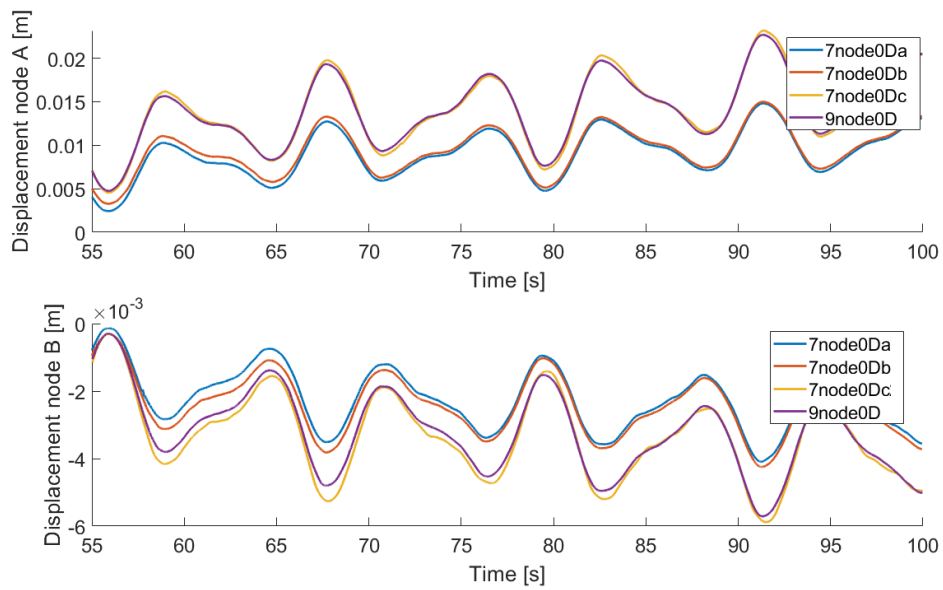Figure A.17: Pore water pressure under impulse load

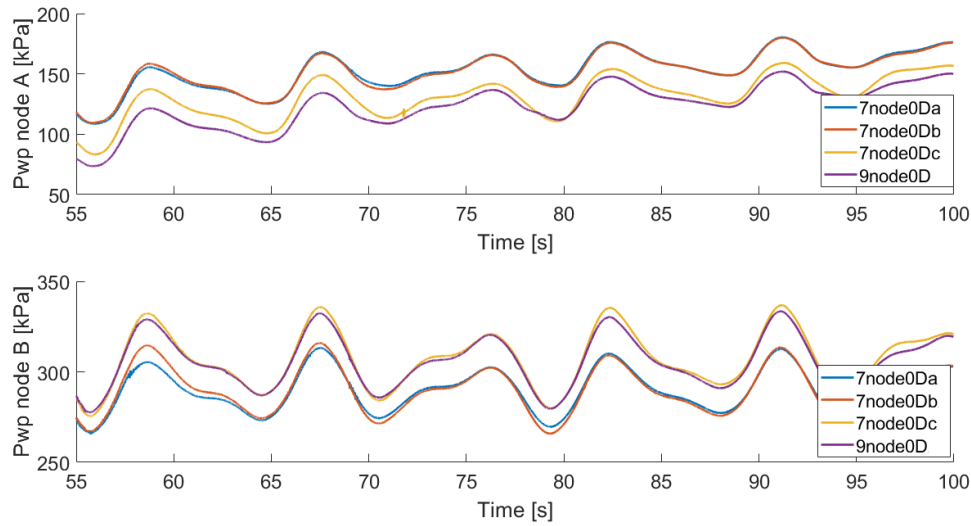Figure A.18: Local displacement under sine load 2

Figure A.19: Pore water pressure under sine load 2

Thus overall, the cyclic behaviour of the soil is assumed to be of a similar nature and this does not form a decisive factor in the mesh selection. Thus, the final mesh selection is largely dependent on the pore water pressure and local displacement behaviour, as the chosen nodes are such that their positions correspond very closely.

Based on the greater number of elements and better element distribution, the mesh D can be assumed to be most accurate of the chosen meshes. In comparing the other meshes to mesh D, it can be noted in figures A.16 and A.17, that the behaviour of mesh C (denoted as 7node0Dc in figure), corresponds most closely to that of mesh D. This is evident in the figures A.16 to A.19. In the latter figures specifically, where the F_{mean} is non-zero, this is all the more evident that as mean response as well as the deviation response of meshes C and D match much better than mesh A or mesh B. Thus the behaviour of a denser mesh is achieved with a much lower computational time (refer table **??**) with mesh C.

As noted earlier, the mesh C results are applicable to both meshes C0 and C2, in figures A.4 and A.5. Mesh C0 offers an exclusive advantage in that its element distribution most closely replicates the 1D scour model (described in the following section, figure A.20), by representing the densification in the top layers of the mesh, as seen in the scour model. However, during the full simulations, mesh C2 is found to be more stable. Thus, the mesh C2 is finally used in simulations.

A.2. Scoured mesh

The scoured mesh (local scour) is produced by maintaining parameters as close to the no scour condition as far as possible. This is achieved by an excavation in the upper densified section of the mesh C0 (the depth of this section is the same as 1D scour). In case of 1D global scour, this layer (between 0 - 9 m depth from mudline) is removed altogether. Thus, the no-scour, global 1D scour, and local 1D scour versions of the mesh are created and visualized in figures A.5, A.20 and A.21.
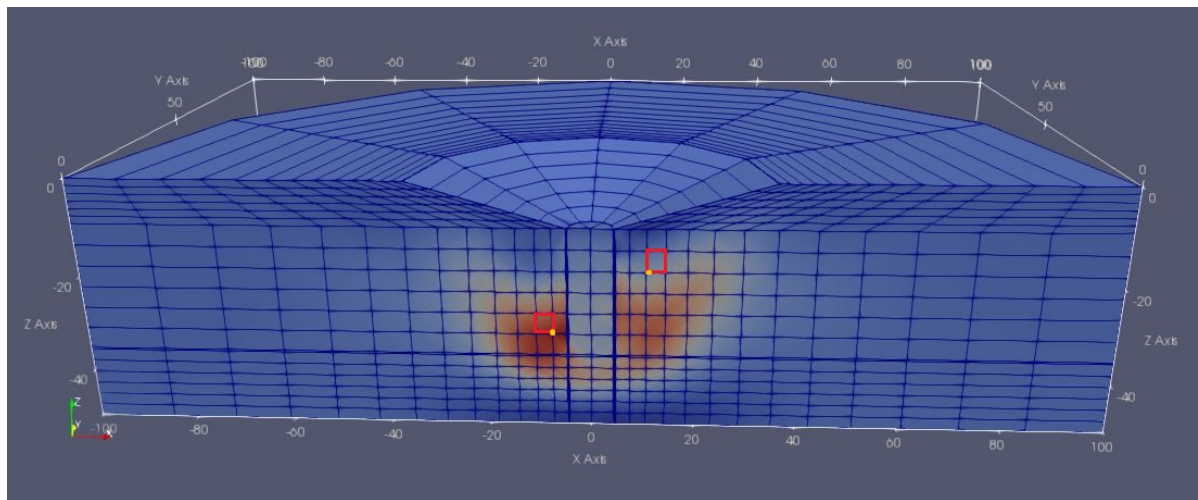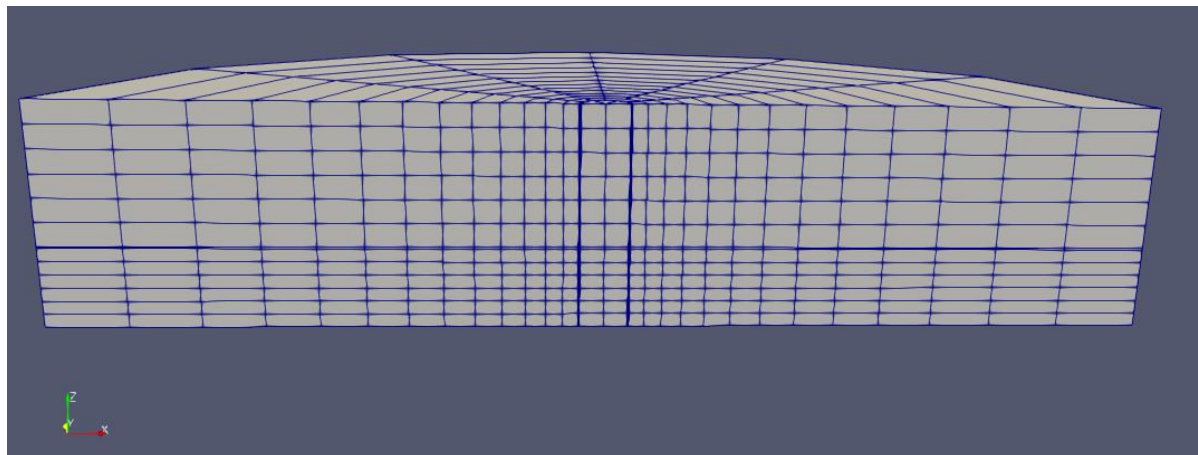

Figure A.20: Mesh C with 1D local scour

Figure A.21: Mesh C with 1D global scour

The cyclic soil behaviour of the mesh with local scour (at control points and elements marked in figure A.20) is also shown in figures A.22 to A.25. The cyclic response is found to be similar to the expected response (based on knowledge of no scour condition), and thus this mesh can be deemed acceptable.

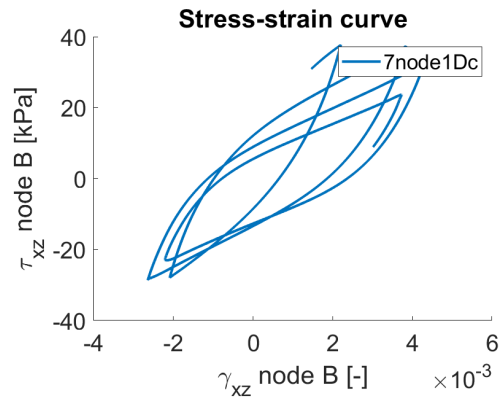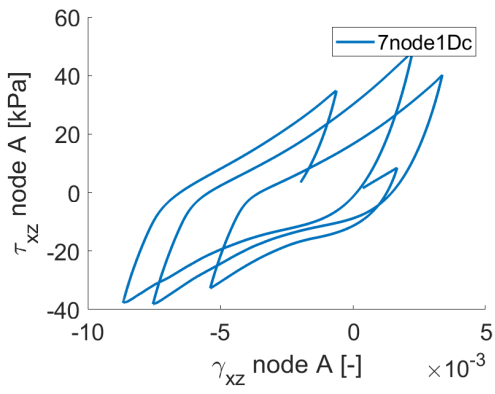Figure A.22: Stress-strain behaviour at element A under sine load 1   Figure A.23: Stress-strain behaviour at element B under sine load 1
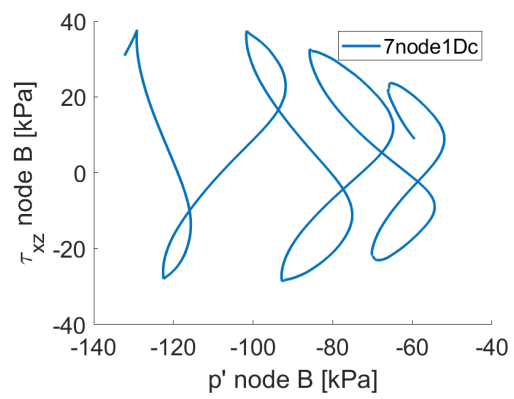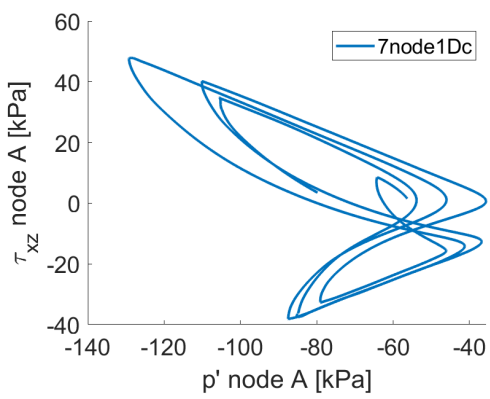

Figure A.24: τ_{xz}-p' element A under sine load 1   Figure A.25: τ_{xz}-p' element B under sine load 1

The mesh for global scour is quite similar to those generated for no scour condition, and thus is not deemed to require separate validation tests.

B

Timoshenko beam section properties

The tower of the DTU 10MW turbine is divided into 22 sections. The first 12 sections are of length $1m$ each - this allows for nodes with $1m$ spacing where the wave loading can be applied, in case of wave heights above still water level. Realistically however, wave loading is applied to only up to $5-6m$ above the still water level. The remaining tower is divided into 10 sections. The sectional properties of the tower, as applied to the model, is given in table B.1 below. Here, $0m$ indicates the still water level. Below still water depth up to mudline, the section properties are uniform, corresponding to that of the monopile. The section properties of each of these sections is listed in the forst row of the table B.1. IT SHO

Table B.1: Section properties of tower

Bottom height [m]	Top height [m]	Mass/L [t/m]	A [m^2]	Jx [m^4]	I [m^4]	A_ν [m^2]	Thickness [m]	Outer diameter [m]
Monopile (-20 to 0 m)		12.21	1.55	30.35	15.18	1.29	0.110	9.00
0.000	1.000	8.384	0.986	33.664	8.416	1.644	0.038	8.300
1.000	2.000	16.711	1.966	66.670	16.668	3.277	0.038	8.272
2.000	3.000	14.934	1.757	59.463	14.866	2.928	0.038	8.261
3.000	4.000	15.222	1.791	60.471	15.118	2.985	0.038	8.248
4.000	5.000	15.098	1.776	59.872	14.968	2.960	0.038	8.236
5.000	6.000	15.058	1.771	59.609	14.902	2.952	0.038	8.223
6.000	7.000	15.002	1.765	59.311	14.828	2.942	0.038	8.210
7.000	8.000	14.665	1.725	57.675	14.419	2.875	0.038	8.128
8.000	9.000	14.628	1.721	57.582	14.396	2.868	0.038	8.108
9.000	10.000	14.536	1.710	57.242	14.310	2.850	0.038	8.082
10.000	11.000	14.461	1.701	57.002	14.250	2.836	0.038	8.056
11.000	12.000	8.101	0.953	30.374	7.593	1.588	0.038	8.022
12.000	23.000	7.543	0.887	27.342	6.836	1.479	0.036	7.882
23.000	34.500	7.204	0.848	25.178	6.295	1.413	0.035	7.743
34.500	46.000	6.873	0.809	23.190	5.798	1.348	0.034	7.604
46.000	57.500	6.549	0.770	21.275	5.319	1.284	0.033	7.465
57.500	69.000	6.232	0.733	19.522	4.881	1.222	0.032	7.325
69.000	80.500	4.488	0.528	11.046	2.761	0.880	0.026	6.490
80.500	92.000	3.965	0.467	8.944	2.236	0.778	0.024	6.211
92.000	103.500	3.473	0.409	7.149	1.787	0.681	0.022	5.933
103.500	115.625	3.005	0.354	5.608	1.402	0.589	0.020	5.647
115.625	119.000	2.927	0.344	5.170	1.293	0.574	0.020	5.500